MEDICAL IMAGE SEGMENTATION

by

FELICIA S. JONES

(Under the Direction of Hamid Arabnia)

ABSTRACT

The National Library of Medicine's Visible Human Project is a digital image library containing full color anatomical, CT and MR images representing an adult male and female. Segmentation of the Visible Human datasets offers many additions to the original goal of a three-dimensional representation of a computer generated anatomical model of the human body. This paper presents an automatic segmentation algorithm called the Medical Image Segmentation Technique, MIST, which is based on a seeded region growing approach. The technique repeatedly extracts anatomical regions of interest from two-dimensional cross section images to create three-dimensional visualizations of these anatomical organs, bones and tissues. Resulting segmentations of this technique are compared with existing segmentation algorithms. This method proves to produce better whole organ and tissue segmentations than existing algorithms.

INDEX WORDS: Image segmentation, Anatomical feature extraction, Seeded region growing

MEDICAL IMAGE SEGMENTATION

by

FELICIA S. JONES

B.A., DePauw University, 2001

A Thesis Submitted to the Graduate Faculty of The University of Georgia in Partial

Fulfillment of the Requirements for the Degree

MASTER OF SCIENCE

ATHENS, GEORGIA

2003

MEDICAL IMAGE SEGMENTATION

by

FELICIA S. JONES

Major Professor:	Hamid Arabnia
Committee:	Liming Cai Thiab Taha

Electronic Version Approved:

Maureen Grasso
Dean of the Graduate School
The University of Georgia
August 2003

DEDICATION

To those who have encouraged me to never give up.

ACKNOWLEDGEMENTS

I thank GOD for helping me through this stage of my life. I would like to thank Dr. Hamid Arabnia for his encouragement and constant academic support. I am also grateful to Dr. Liming Cai and Dr. Thiab Taha for their many thoughtful suggestions. The Department of University Housing also deserves special recognition for creating a supportive working environment enabling me to complete my degree.

TABLE OF CONTENTS

Page

CHAPTER

APPENDIX

CHAPTER 1

INTRODUCTION

The most common images used in medicine are the CT and MR images. X-ray computed tomography (CT, or CAT for computer assisted tomography) involves an X-ray source and a detector positioned on opposite sides of a patient. The equipment is arranged in such a way that the X-ray beam can be rotated about one axis while the patient is translated parallel to that axis. In this way, X-ray images of each section are digitally recorded from many angles. Subsequently, algorithms derived from a mathematical procedure called tomography are applied to reconstruct a three-dimensional matrix of values representing the X-ray transmission properties in the volume occupied by the specimen [19].

Magnetic-resonance imaging (MRI) is an imaging technique used primarily in medical settings to produce high quality images of the inside of the human body. A MRI is similar to CT, but it does not use X-rays. Instead, a strong, magnetic field is used to affect the orientation of protons, which behave like miniature magnets and tend to align themselves with the external field.

Anatomical images are also used in the medical domain. The National Library of Medicine's (NLM) Visible Human Project ® (VHP) is the creation of complete, anatomically detailed, three-dimensional representations of the normal male and female human bodies. The male cadaver was sectioned at 1-millimeter intervals, the female cadaver at .33-millimeter intervals. The anatomical images in this dataset are full color 24-bit cross section images that show the detail of the human body [1].

The dataset includes digitized photographic images from cross-sectioning, digital images derived from computerized tomography (CT) and digital magnetic resonance (MR) images of human cadavers. The male dataset consists of 1,871 cross sections for each mode, anatomical and CT, while the female dataset consists of 5,189 anatomical images. Both the male and female datasets contain axial images of the entire body in the anatomical and CT mode; the MR mode contains axial images of the head and neck areas and longitudinal sections of the rest of the body obtained at 4mm intervals [1].

To date, researchers from all over the world have used the dataset for medical diagnostic and treatment applications, as well as for educational purposes for students of all ages [1,7]. Image segmentation and anatomical feature extraction is a widely researched area related to the use of the dataset.

1.1 Objective of Thesis

One of the most important problems in image processing and analysis is segmentation [12, 13, 17]. This thesis presents a new segmentation method called the Medical Image Segmentation Technique (MIST), used to extract an anatomical object of interest from a stack of sequential full color, two-dimensional medical images from the Visible Human dataset. We use the segmented regions from each image to achieve our objective of forming a three-dimensional visual representation of the object of interest. The quality of the visualization of the 3D structure is highly dependant on the success of the segmentation algorithm used to extract the object from the 2D images. Therefore, while

3D visualization is our ultimate goal, it cannot be achieved without strong emphasis on addressing the issue of image segmentation.

1.2 Organization of Thesis

Chapter 2 discusses related work in the area of segmentation applications to the Visible Human Project. Traditional segmentation methods and other existing segmentation algorithms that have been applied to the VHP dataset are reviewed in Chapter 3. The problems associated applying these methods to the VHP's anatomical images are also discussed. The experiments show that these segmentation algorithms are not good enough for the goals of our application. A new segmentation technique, Medical Image Segmentation Technique (MIST), is introduced in Chapter 4. A comprehensive methodology of this technique is presented. Chapter 5 displays the results of MIST as well as a comparison to other segmentation techniques. The experiments in this section show that MIST is more effective in producing three-dimensional representations of anatomical objects over other segmentation methods considered in Chapter 3. Conclusions and future refinements for our work are presented in Chapter 6.

CHAPTER 2

PREVIOUS WORK

Research in medical informatics concentrates primarily on integrating computer technology into the practice of medicine to improve all areas of the field from education to diagnosis and treatment [6]. The Visible Human Project at the NLM is designed to serve as a common reference for the study of human anatomy, as a set of common public domain data for testing medical imaging algorithms, and as a test bed and model for the construction of image libraries that can be accessed through networks [1]. Currently, the dataset is being applied to a wide range of educational, diagnostic, treatment planning, virtual reality, artistic, mathematical and industrial. Many browsers and other applications have been designed to display the images of the Visible Human Dataset.

The NPAC Visible Human Viewer [22] developed at Syracuse University, was the first online viewer developed for visualizing the VHP dataset. This Java applet allows users to select and view two-dimensional images of the human body from 3 different angles. There have been many enhancements to the viewer since its debut in 1995.

The National Library of Medicine has also contributed to the development of image browsers for the dataset. The AnatQuest project is a web based interface for viewing the Visible Human anatomical slices, as well as rendered anatomical organs [23]. Users have the ability to browse images through an adjustable size viewing area, downloading portions of the image to the browser as needed. AnatLine is a prototype system consisting of an online, java based database and image browser. AnatLine allows users to download anatomically labeled slices from the thorax region of the Male dataset. Images used in AnatQuest and AnatLine are scanned from 70mm color photographs of the male cadaver. At the time of its development the thorax region was the only labeled area of the dataset.

Researchers at the Swiss Federal Institute of Technology in Lausanne, Switzerland have developed many applications for viewing the images in the Visible Human dataset. The Visible Human Slice Sequence Animation Web Server is a web-based service for extracting slices, curved surfaces and slice animations from the Visible Human dataset [20]. The application also allows users to construct 3D anatomical scenes using combinations of slices from the dataset and 3D models of internal structures, and extract 3D animations.

The real-time interactive visible human navigator was also developed at the Swiss Federal Institute of Technology [21]. This application has the ability to extract arbitrarily oriented and positioned slices from the Visible Human dataset in real-time. A continuous sequence of slices is displayed in real-time in response to navigation commands from the user.

Papers addressing the specific problem of segmentation in medical imaging include an automated 3D region growing algorithm proposed by Chantal Revol-Muller et al [2]. This method, applied to 3D MR images of human bone samples, is used to diagnose osteoporosis. The region growing algorithm uses a homogeneity threshold that increases from a very small value to a large value for each input image. The segmentations are evaluated to determine the optimal homogeneity value and proves to be more successful than other automatic and manual thresholding methods.

A semi-automated segmentation method proposed by C. Imelinska et al. [6, 27], repeatedly divides an input image into regions using Voronoi diagrams. The algorithm classifies the regions of anatomical tissues based on classification statistics. This work was the first attempt at outlining fine anatomical structures in color medical images.

To create a three-dimensional model of the human body, researches at the University of Geneva developed the Comprehensive Human Animation Resource Model (CHARM) [24]. The CHARM project is an attempt at providing a structured and dynamic model of the body in contrast to the unstructured and static data provided by the Visible Human dataset. Two-dimensional contours are segmented from anatomical and CT images to form 3D surfaces of the upper left limb. CHARM includes a labeling tool for identifying each organ of interest in the 2D images.

The Visible Human project has also led to the creation of similar projects as the Visible Embryo and the Visible Animal Project. The Visible Embryo Project [25], officially called the Human Embryology Digital Library and Collaboratory Support Tool, is a collaborative effort by the National Library of Medicine' s Communications Engineering Branch, the Human Developmental Anatomy Center at the National Museum of Health and Medicine and the National Institute of Child and Human Development that consists of 10,000 human embryos spanning the 23 stages of embryo development. Similar to one of the goals of the Visible Human Project, the emphasis of this project is to provide data from this collection of biomedical information to researchers and students over the World Wide Web.

The Visible Animal Project [26] is made up of anatomical, CT and MR images of a mature dog. For the first time a complete high-resolution three-dimensional database of a dog is available, which can be used as the base for further high quality three-dimensional reconstructions.

CHAPTER 3

SEGMENTATION TECHNIQUES

3.1 Introduction

Segmentation is one of the most important techniques for image processing [15]. The purpose of segmentation is to partition an image into distinct, semantically meaningful entities by defining boundaries between features and objects in an image based on some constraint, or homogeneity predicate. Specifically, the segmentation problem is defined as sufficiently partitioning an image into non-overlapping regions. Segmentation can therefore be formally defined as follows:

If F is the set of all pixels and P( ) is a homogeneity predicate defined on groups of connected pixels, then segmentation is a partitioning of the set F into a set of connected subsets or regions ($S_1, S_2, \ldots, S_n$) *such that:*

$$\bigcup_{i=1}^{n} S_i = F \;\; with \;\; S_i \cap S_j = \varnothing, \qquad i \neq j .$$

The homogeneity predicate $P(S_i)$ = *true for all regions* (S_i) *and*

$P(S_i \cup S_j)$=*false , when* S_i *is adjacent to* S_j [18].

Homogeneity predicates are usually based on image intensity, color, texture, etc. According to Harlick and Shapiro [3], image segmentation can be classified into these categories: spatial clustering, split and merge schemes, and region growing schemes.

3.2 Spatial Clustering

Haralick and Shapiro [3] present that the difference between clustering and segmentation is that in image segmentation, grouping is done in the spatial domain of the image, while clustering is done in measurement space. It is also possible for clustering to result in overlapping regions, while that is not the case for segmentation results. Clustering and spatial segmentation can be combined to form spatial clustering, which combine histogram techniques with spatial linkage techniques for better results.

3.3 Split and Merge Segmentation

Regions in an image are a group of connected pixels with similar properties [5]. The split method begins with the entire image, and repeatedly splits each segment into quarters if the homogeneity criterion is not satisfied. These splits can sometimes divide portions of one object. The merge method joins adjacent segments of the same object.

In intensity based segmentation, the boundaries that separate regions may need to be redefined due to under- or over-segmentation of regions. Split and merge segmentation can also handle this task. Under-segmented regions are corrected by adding boundaries to, or splitting, certain regions that contain parts of different objects. Over-segmented regions are corrected by eliminating false boundaries and merging adjacent regions if they belong to the same object or feature.

3.4 Region Growing

The focus of the remainder of this thesis will be with this class of segmentation. Region growing has shown to be a very useful and efficient segmentation technique in image processing [5, 15]. Region growing in its simplest sense is the process of joining neighboring points into larger regions [16] based on some condition or selection of a threshold value. Seeded region growing starts with one or more seed points and then grows the region to form a larger region satisfying some homogeneity constraint. The homogeneity of a region can be dependent upon any characteristic of the region in the image: texture, color or average intensity. One specific approach to region growing is described in the next section.

3.5 A Comparable Segmentation Approach

Newman et al. [7, 9] discuss a method for volumetric segmentation used for a system designed for diagnosis and surgical planning in medical images. The segmentation results produced by this technique will be compared with the results from our technique in chapter 5.

3.5.1 Definitions

Before discussing the algorithm, a few terms need to be defined:

Definition 1: A *voxel* is the 3D unit for a pixel in a 2D image. We will use the terms interchangeably throughout this report. Region growing, defined earlier, and volume growing will also be used interchangeably, as volume growing is the 3D version of 2D region growing.

Definition 2: *Dilation* is defined as the union of all vector additions of all pixels *a* in object *A* with all pixels *b* in the structuring function *B*. Thus, $A \oplus B = \{t \in Z^2 :\ t = a + b,$ $a \in A$ and $b \in B\ \}$, where the vector t is an element of the image space Z^2 and $a+b$ is the translation of *a* by *b* [11].

Definition 3: *Erosion* is defined as the complement of the resulting dilation of the complement of object A with structuring element B. Thus, A B = $\left(A^C \oplus B\right)^C$ = $\{t \in Z^2 :$ $t + b \in A$ for every $b \in B\ \}$[11].

3.5.2 Newman's algorithm

Given a user-selected seed voxel (pixel) *V* within a structure of interest, the algorithm grows an object using volumetric region growing. The algorithm computes the median voxel value *M* in a three-dimensional 3x3x3 pixel window about *V* as the seed value for volume growing. The value and location of *M* is used as the actual seed for region growing to improve robustness. The median of the window is used to eliminate the problem where the selection of the seed voxel is corrupted by noise. The 3x3x3 window includes voxels in image slices above and below the current image slice.

Voxels whose intensity values are within *t* units of the median window value *M* are said to be a part of the region. The static value for the parameter, *t*, is automatically chosen from a database based on the type of tissue to be extracted (bones, organs, internal organ structures, and tumors and cysts). Since tissues of the same types tend to exhibit homogeneous values, Newman, et. al was able to select permanent thresholds for each tissue.

3.5.3 Morphological Refinement

After volume growing, Newman's algorithm uses morphology operations to improve the initial coarse segmentation resulting from the procedure described in the previous section.

Binary dilation of an object increases its geometrical area by setting the background pixels adjacent to an object's contour to the objects intensity value. Binary erosion of an object reduces its geometrical area by setting the contour pixels of an object to the background value [11]. Erosion followed by dilation with the same structuring element will remove all of the pixels in regions that are too small to contain the structuring element, and it will leave the rest. This operation is referred to as closing.

Newman's algorithm performs a 3D close operation followed by a single dilation on the region produced by the initial coarse segmentation. The close operation removes isolated interior voxels that are initially present in the region. The single dilation is used to expand the region boundary. Morphological refinement reduces the gaps and holes that are visible in initial segmentations. The algorithm steps are shown in Figure 2.1.

3.5.4 Results

This method produces some problematic segmentations. A number of gaps and holes are present in the segmented structures even after they were altered with morphological operations. In addition, [7] reported that the segmented region could become disconnected through the closing and dilation morphological operators. For our application, a better segmentation with fewer gaps and holes is desired. A more sophisticated segmentation technique is required to achieve our goals.

```
Volume_Grow();

    Let W be the set of dataset voxels and t be a threshold on magnitude difference
    S = {};
    Choose seed voxel w0 with intensity |w0|.
    Determine median intensity I in the window of voxels about w0.
    Recursive_Region_Grow(W, S, w0, I, t).
    Remove Isolated Interior Voxels; Close.
    Expand Region Boundary; Dilate One Voxel.

Recursive_Volume_Grow( W, S, w0, I, t):
    S = S+W.
    If $w_i \in W$ adjacent to $w_0$, $w_i \notin S$, and
    if $|I| - |w_i| < t$ then
            Recursive_Region_Grow($W$, $S$, $w_i$, $I$, $t$).
```

Figure 3.1: Volume-Growing Algorithm [7].

CHAPTER 4

MIST: MEDICAL IMAGE SEGMENTATION TECHNIQUE

4.1 Introduction

In this chapter, we describe an automatic segmentation technique used in the Medical Image Segmentation Tool (MIST), and applied to the Visible Human's cross-section data. Figure 4.1 shows how the resulting algorithm extracts regions of organs, muscles and tissues from full color two-dimensional (2D) cross section images of a frozen cadaver, slice-by-slice, to create three-dimensional (3D) visualizations of these anatomical areas of interest. The segmentation algorithm assumes minimal knowledge about the organ or muscle tissue to be extracted. The user supplies the initial seed pixel that identifies the region of interest. This region of interest is then segmented from a stack of sequential 2D cross section images using a seeded region growing approach.

4.2 Initial Approach to MIST

The initial approach to solving the segmentation problem in this application was to use a technique that would produce closed contours of the anatomical objects in the image. The idea of a closed contour simplifies the segmentation process. Once the user identifies the region of interest by supplying a seed point, whichever contour contained that point is identified as the object of interest. Next, a contour filling algorithm would be used to extract only this area from the rest of the image, using the closed contour as the boundary.

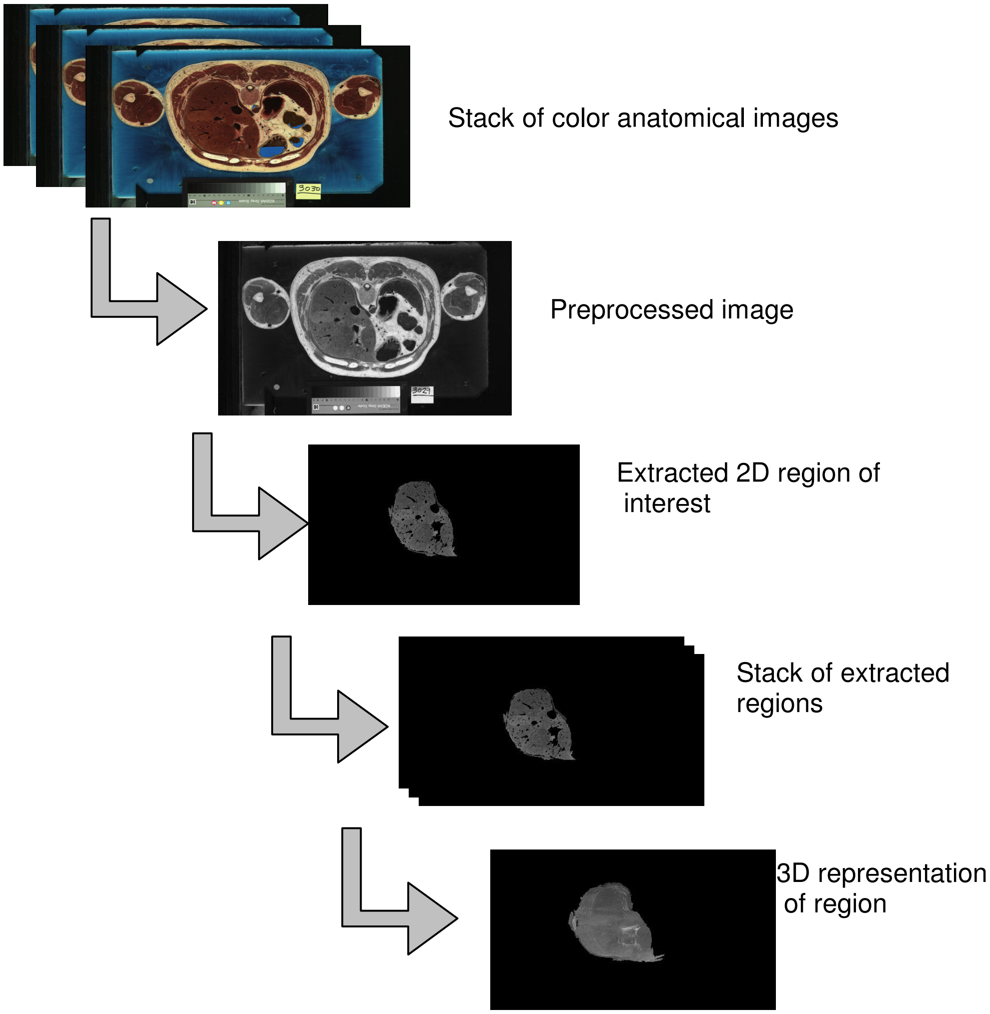

Figure 4.1: Flowchart of process

4.2.1 Standard Edge Detection

To use this approach, we examined a number of standard edge detectors. The goal was to find the "best" edge detector for our application. The best edge detector is the one that produce a closed contour of one pixel thick edges.

In gradient edge detection methods, the assumption is that edges are formed by pixels with a high gradient. A fast rate of change of intensity at some direction given by the angle of the gradient vector is observed at edge pixels. The magnitude of the gradient indicates the strength of the edge. All of the edge detectors in the gradient class approximate the first derivative. A common disadvantage of these operators is their failure to provide reliable segmentation due to their gradient-based nature. In the following descriptions, *(x,y)* represents the pixel location in the input image.

Roberts Operator

$$\mathrm{G_x} = \begin{bmatrix} 1 & 0 \\ 0 & -1 \end{bmatrix} \qquad \mathrm{G_y} = \begin{bmatrix} 0 & -1 \\ 1 & 0 \end{bmatrix}$$

The above masks are convoluted on the original image by computing $G[I[x,y]] = |G_x| + |G_y|$ for the Roberts Operator [5], where *I[x,y]* represents the input image. The mask computes the difference between a pixel and its vertical and horizontal neighbors at the interpolated point, $[i+\frac{1}{2}, j+\frac{1}{2}]$. The results of the Roberts Operator are shown in the figures at the end of this section.

Sobel Operator

The Sobel operator [5] is often used as a detector of horizontal and vertical edges.

$$\mathrm{x} = \begin{bmatrix} -1 & 0 & 1 \\ -2 & 0 & 2 \\ -1 & 0 & 1 \end{bmatrix} \qquad \mathrm{y} = \begin{bmatrix} 1 & 2 & 1 \\ 0 & 0 & 0 \\ -1 & -2 & -1 \end{bmatrix}$$

Edge strength or magnitude is derived as:

$$\sqrt{x^2 + y^2} \quad \text{or} \quad |\mathrm{x}| + |\mathrm{y}|$$

and the direction is derived as:

$$tan^{-1}(y/x)$$

This operator places an emphasis on pixels that are closer to the middle of the masks. The performance of this operator is shown in figures at the end of this section.

Prewitt Operator

The Prewitt operator [5] highlights vertical (convolution x) and horizontal (convolution y) boundaries.

$$\mathrm{x} = \begin{bmatrix} -1 & 1 & 1 \\ -1 & -2 & 1 \\ -1 & 1 & 1 \end{bmatrix} \qquad \mathrm{y} = \begin{bmatrix} 1 & 1 & 1 \\ 1 & -2 & 1 \\ -1 & -1 & -1 \end{bmatrix}$$

This operator is similar to the Sobel operator with the exception of the emphasis at the center of the mask. The direction and edge magnitude image are obtained using the same formulas as the Sobel operator.

The compass operators [8, 15] are an alternative approach to the differential gradient edge detectors. This operation estimates the local edge gradient of the input image. The input image is convolved with a set of 8 convolution kernels, each of which is sensitive to edge in a different orientation. For each pixel *(i,j)* , the local edge gradient magnitude is estimated with the maximum response of all 8 kernels at this pixel location. The final gradient image G is computed to be:

$$|G| = max(|G_i|: i=1 \text{ to } 8)$$

where G_i is the response of the kernel i at the particular pixel position. The result for the edge magnitude image is so determined by the template that matches the local area of the pixel the best. The 8 kernels are shown here using the Prewitt mask, with their respective orientations:

$$\begin{bmatrix} -1 & 1 & 1 \\ -1 & -2 & 1 \\ -1 & 1 & 1 \end{bmatrix} \quad \begin{bmatrix} 1 & 1 & 1 \\ -1 & -2 & 1 \\ -1 & -1 & 1 \end{bmatrix} \quad \begin{bmatrix} 1 & 1 & 1 \\ 1 & -2 & 1 \\ -1 & -1 & -1 \end{bmatrix} \quad \begin{bmatrix} 1 & 1 & 1 \\ 1 & -2 & -1 \\ 1 & -1 & -1 \end{bmatrix}$$

$$0^{o} \qquad 45^{o} \qquad 90^{o} \qquad 135^{o}$$

$$\begin{bmatrix} 1 & 1 & -1 \\ 1 & -2 & -1 \\ 1 & 1 & -1 \end{bmatrix} \quad \begin{bmatrix} 1 & -1 & -1 \\ 1 & -2 & -1 \\ 1 & 1 & 1 \end{bmatrix} \quad \begin{bmatrix} -1 & -1 & -1 \\ 1 & -2 & 1 \\ 1 & 1 & 1 \end{bmatrix} \quad \begin{bmatrix} -1 & -1 & 1 \\ -1 & -2 & 1 \\ 1 & 1 & 1 \end{bmatrix}$$

$$180^{o} \qquad 225^{o} \qquad 270^{o} \qquad 315^{o}$$

The results of this operator are shown in figures at the end of this section.

Laplacian Operator

The Laplacian operator [5, 15] approximates the second derivative, which gives the gradient magnitude, or direction.

One disadvantage of the Laplacian operator is that it can produce thick edges in an image. This edge detector typically has two different masks, one for 4-neighborhoods and one for 8-neighborhoods, both shown below:

For 4-neighborhoods:

$$\nabla^2 = \begin{bmatrix} 0 & 1 & 0 \\ 1 & -4 & 1 \\ 0 & 1 & 0 \end{bmatrix}$$

For 8-neighborhoods:

$$\nabla^2 = \begin{bmatrix} 1 & 1 & 1 \\ 1 & -8 & 1 \\ 1 & 1 & 1 \end{bmatrix}$$

Laplacian of Gaussian

The Laplacian of Gaussian (LoG) [5, 15] is considered to be the optimal standard edge detector. This is because it performs a Gaussian smoothing on the image before applying the Laplacian edge detector. The mask is convoluted on the image for optimal results. The convolution mask of a LoG operator is:

$$\nabla^2 h(x,y) = \left(\frac{x^2 + y^2 - \sigma^2}{\sigma^4} \right) e^{-\frac{x^2+y^2}{2\sigma^2}} \qquad [5].$$

The Multi-scale Laplacian of Gaussian procedure performs better than edge detection based on image filtering with a single scale. Single scale edge detectors may result in the over- or under-detection of edges when images are corrupted by noise, which leads to incorrect edge detection.

This procedure is also known as Bergholm's edge focusing algorithm. The guiding principle in this process is to detect significant edges at a large scale. This will suppress the noisy edges, however significant edges will be dislocated. The procedure tracks significant edges for successively lower scales. If the change in scale is less than ½, then the edges are not displaced by more than one pixel between successive scales.

For the first iteration of the LoG operator on an input image, edges are to be detected at a high scale. Then for successively lower scales edges are detected only where they were detected at the previous scale and the edge's 8-pixel neighborhood. This is done because the edges will not be displaced by more than one pixel.

Canny Operator

The Canny operator [5, 15] closely approximates the operator that optimizes the product of signal-to-noise ratio and localization. Let *S[i,j]* be the result of convolving the input image, *I[i,j]*, with a gaussian smoothing filter given by:

$$S[i,j] = G[i,j,\sigma] * I[i,j]$$

The gradient of *S[i,j]* is computed to produce two arrays P[i,j] and Q[i,j] for the x and y partial derivatives:

$$P[i,j] \approx (S[i,j+1] - S[i,j] + S[i+1,j+1] - S[i+1,j])/2$$

$$Q[i,j] \approx (S[i,j] - S[i+1,j] + S[i,j+1] - S[i+1,j+1])/2$$

The magnitude and orientation of the gradient can be computed from:

$$M[i,j] = \sqrt{P[i,j]^2 + Q[i,j]^2} \quad \text{and} \quad \theta[i,j] = \arctan(Q[i,j], P[i,j])$$

respectively.

4.2.2 Results of the Standard Edge Detectors

The performance of the standard edge detectors is displayed in this section. Figure 4.2 shows an original image taken from the thorax region of the male dataset used to test the performance of the standard edge detectors. Figure 4.3a-h show the performance of the Roberts, Sobel, Prewitt, compass, Laplacian, Laplacian of Gaussian and Canny operators on the images shown in Figure 4.2. Edges were detected for each color component and the resulting images were thresholded to obtain an edge map. The

Roberts operator detects thin edges while keeping the original detail in the image. The edges detected by the Sobel, Prewitt, compass and Canny operators are similar in that they detect edges on the outside boundary of the abdomen, but the more detailed parts of the images are not as distinct. The resulting edge map obtained from performing the LoG operator on the input image accurately detects edges along the boundary of the region of interest. However, these edges are not guaranteed to be a part of a closed contour of the region. The multi-scale LoG operator produces disconnected edges and the edges are not detected along the boundaries of the organs in the image.

Our goal of obtaining edges thinner than those presented in the images in Figure 4.3 could have been achieved at the cost of loss of detail by increasing the threshold value, so that fewer false edges would be detected. Additionally, none of the standard edge detectors produce closed contours of our region of the region of interest in the input image.

Anatomical images, in general, contain many detailed aspects as well as noise. It is hard to find an edge detector that will optimally find the edges while removing noise. In these types of images, a different segmentation method is needed to analyze a specific area of interest in the image. The noise and the important aspects in the image are not very distinguishable, even by the human eye.

4.2.3 Non-linear Laplace Algorithm

The non-linear Laplace edge detector proposed by Vliet and Young [11,12], was also investigated. This algorithm uses a non-linear Laplace operator and the Marr-Hildreth model of edge detection. A flow diagram of the model is presented in Figure 4.4.

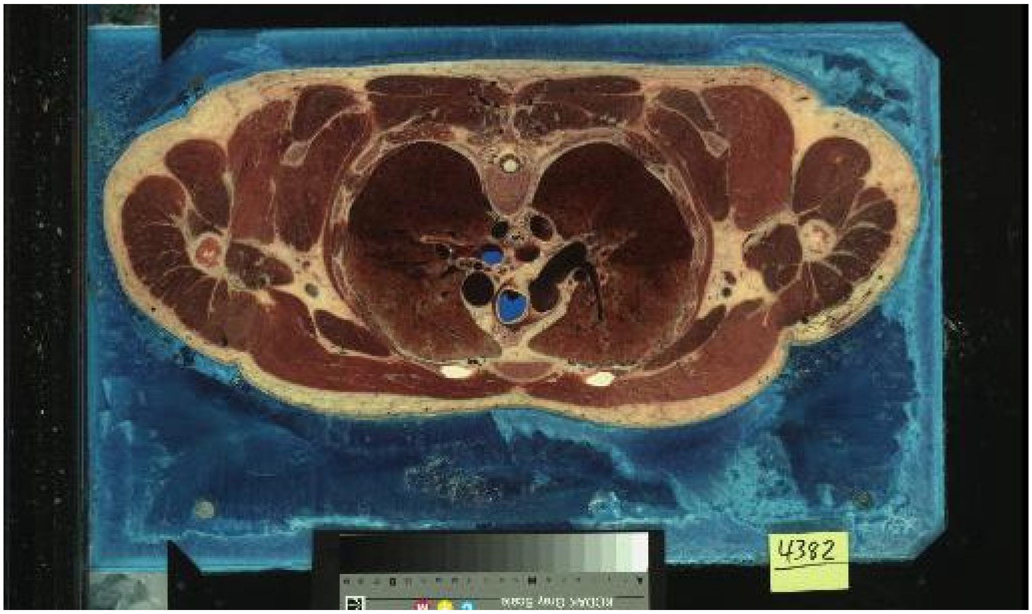

Figure 4.2: Image taken from the thorax region of the male dataset.

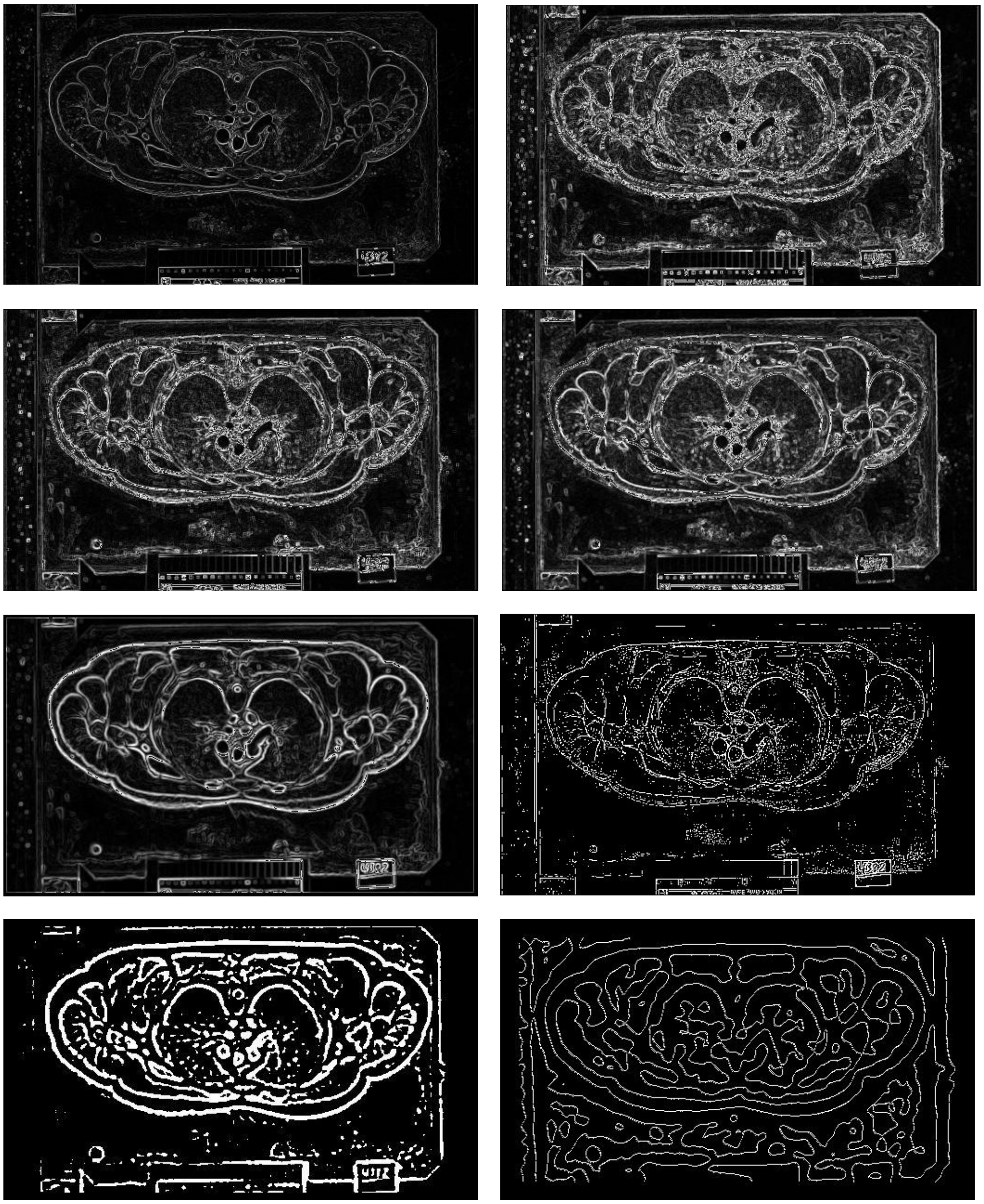

Figure 4.3: The standard edge detection comparison on the anatomical thorax image: (A) edges obtained by Roberts operator, (B) edges obtained by the Sobel operator, (C) edges obtained by the Prewitt operator; (D) edges obtained by the Compass operator; (E) edges obtained by the Canny operator; (F) edges obtained by the Laplacian operator. (G) edges obtained by LoG operator (sigma = 3); (H) edges obtained by the multi-scale LoG operator.

First a smoothing filter is applied to the input image. The algorithm uses a 3x3 Gaussian filter to accomplish this task. Next, they propose a non-linear Laplace operator in place of the traditional Laplace operator represented by :

$$\nabla^2 I(x,y) \approx I(x+1,y) + I(x-1,y) + I(x,y+1) + I(x,y-1) - 4I(x,y)$$

The non-linear Laplace operator is performed on the smoothed image, I, using the following equations:

$$\mathrm{NLLAP}(x,y) = \mathrm{gradmax}(x,y) + \mathrm{gradmin}(x,y)$$

$$\mathrm{gradmax}(x,y) = \mathrm{MAX}_n \{ I(x,y) \} - I(x,y)$$

$$\mathrm{gradmin}(x,y) = \mathrm{MIN}_n \{ I(x,y) \} - I(x,y)$$

where MAX_n and MIN_n are two simple non-linear filters, the local maximum and the local minimum filter with an *nxn* square window as structuring element.

The next step in the edge detection algorithm is to use a zero crossing detector to determine where the Laplace filtered image changes sign. The pixels are separated into three regions, positive, zero and negative. The zero value pixels are assigned to the nearest adjacent region using two distance transformations. The zero crossing detector ensures a maximum displacement of one pixel. The closed contours are found in the zero crossing image, however this only guarantees good performance when dealing with blurred images where long ramp edges often occur.

An edge strength detector is a measure for the steepness of an edge at any location in the input image. Traditional gradient filters such as Roberts, Prewitt and Sobel have the ability to provide edge strength images but perform best when used on images with high signal to noise ratios [11]. Vliet and Young use the following definition for an edge

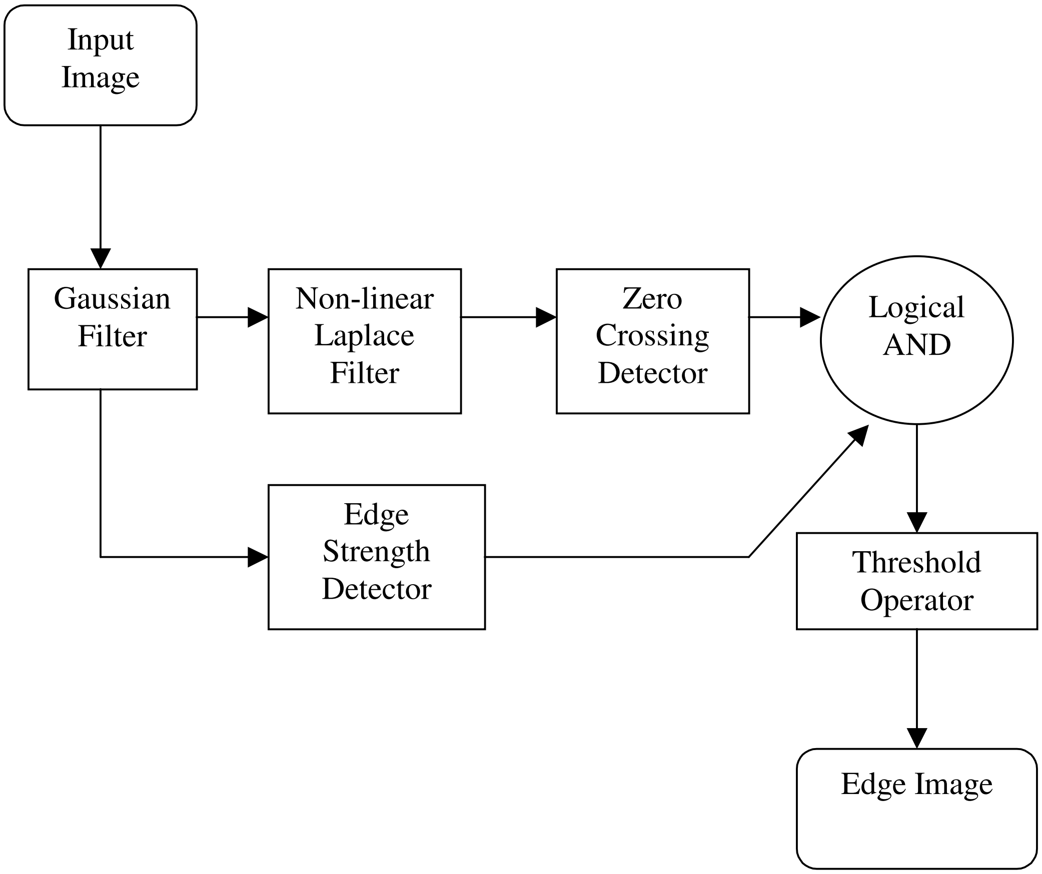

Figure 4.4. The non-linear laplace edge detection model. [11]

strength image:

$$I_{\text{Edge Strength}}(x,y) = \mathbf{min}\{\ \text{gradmax}(x,y), -\text{gradmin}(x,y)\ \}.$$

This equation is based on a morphologic edge detector presented by Lee in [14].

The final step in this edge detection model is to combine the resulting image from the zero crossing detector with the edge strength image, using the logical AND operation, to get an edge image. Specifically, if an edge exists in both the zero crossing image and the edge strength image, then it is considered an edge in the resulting edge image. This edge image represents the likelihood that they belong to an edge in the original image. Using an appropriate threshold value produces closed contours in the final edge image.

4.2.4 Discussion

The standard edge operators did not produce sufficient closed contours for the goals of our technique. The non-linear Laplace operator is extremely effective and flexible in the detection of one pixel thick edges, as shown in the resulting image in Figure 4.5. However, the thresholding required to get the final edge image requires additional information about the anatomical feature to be extracted. Thresholding in itself is a difficult task without prior knowledge of information in the image. We determined that a different segmentation technique would be necessary because the production of closed contours is very highly dependent on the thresholding value chosen to compute the final edge map.

4.3 Region Growing

Region growing was chosen for the MIST application to guarantee segmentation of a closed contour. The seeded region growing algorithm implemented uses a single linkage scheme to merge two neighboring pixels, P_x and P_y, whose intensity values

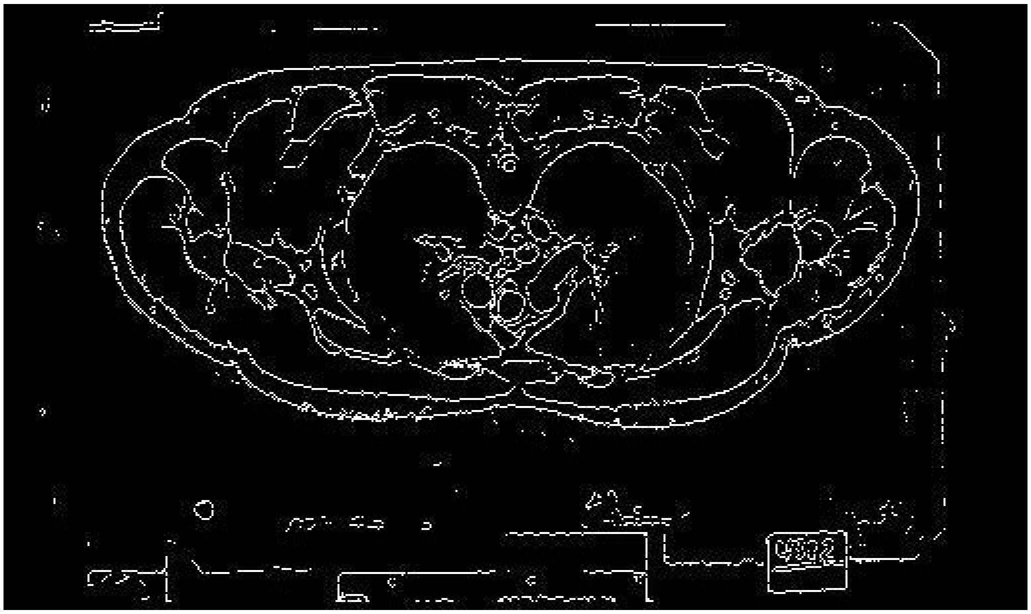

Figure 4.5: Result of the Non-linear Laplace Operator on the image in Figure 4.2.

$f(P_x)$and $f(P_y)$ are sufficiently close, to form a region of interest within the 2D cross section [3]. Adjacent region pixels within a 3x3 neighborhood are said to be a part of the region if the absolute value of their difference is less than α. We have chosen α to be the standard deviation of the histogram of the cross section [2]. This is represented by the equation:

$$\left|f(P_x) - f(P_y)\right| \leq \alpha$$

The pseudo code for the region growing algorithm is shown in Figure 4.6. It maintains a list of candidate points connected to the seed point (x,y), which commences the region growing. We consider each of candidate points in turn. The point, *p*, is said to be part of the region, R, if it satisfies the homogeneity criterion. The algorithm grows the region by adding the neighbors of each point in the region to the set of candidate points and later considering them. Before we add the neighbors of a point, *p*, to the set of candidate points, we mark *p* as already processed to avoid considering it twice. The algorithm returns an integer representing the area, in pixels, of the region of interest, representing the number of pixels in the region.

4.3.1 Definitions and Notations

$I_{1 \dots n}$: Set of anatomical cross section images

$S_{I_{1 \dots n}}$: Set of images containing only segmented regions from cross-sections $\in I$

$A_{S_{1 \dots n}}$: Set of object sizes, in pixels, representing the area of the segmented regions $\in S$

4.3.2 Problem One: The Centroid Problem

One major concern in region growing is the selection of seed pixels. To avoid the necessity of the user choosing a seed pixel for every image slice in the image stack, our

```
int Iterative_Region_Growing (seedPoint p)
{
   candidatePoints = { }
   regionPoints= { }
   p ◊   candidatePoints
   p ◊   regionPoints

   while (candidatePoints.size() != 0 )
    {
         remove first element in candidatePoints and assign it to p;
         if ( p matches the homogeneity criteria) and (p.processed == false)
            {
                  p ◊   regionPoints;
                  p.processed = true;

                   for each neighbor (x, y)  of p
                   {
                           (x,y) ◊   candidatePoints;
                    }
          }
      }
  return regionPoints.size();
}
```

Figure 4.6: Pseudocode for the region growing algorithm

algorithm uses the centroid, or center of mass, of the segmented region as the seed pixel for the next image slice in the sequence. Using the centroid as the seed pixel guarantees that the seed point is contained in the user's region of interest.

Depending on the texture of the anatomical region of interest and the selection of the seed pixel, a basic region growing algorithm can sometimes produce an erroneous segmentation. In the next section we identify these occurrences and present a suitable solution to this problem.

4.3.3 Identifying erroneous segmentations

In Figure 4.7, the liver has been segmented from a cross section image from the thorax region of the Visible Human data. Within the segmented contour of the liver, there are many darker sub-regions, which are not unusual occurrences in a healthy liver. In the image, the centroid of the segmented region is contained in one of the dark areas. Using the centroid as the seed point in this cross section causes the darker sub-region to be identified and segmented as the region of interest, instead of the entire area of the liver. This is due to the location and the intensity of the seed point, as well as the texture of the liver. Because the seed pixel is in a part of the region that is especially dark, the entire liver is not included because the intensity values are not within the range of α, the threshold used in the region growing algorithm.

The resulting segmentation is enhanced in the cross section image in Figure 4.8. The white blob inside the black box in Figure 4.8 represents the segmentation result produced from using the centroid from the previous cross section as the seed point for this cross section. Our algorithm searches for the possible occurrence of this segmentation problem at each iteration of our region growing algorithm. After each 2D cross section image is

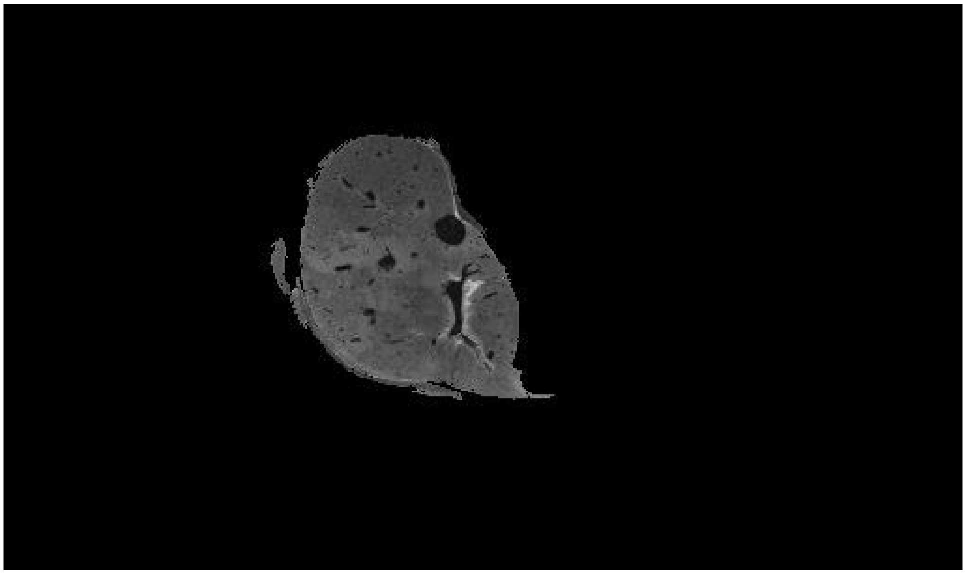

Figure 4.7: Liver extracted from a 2D cross section

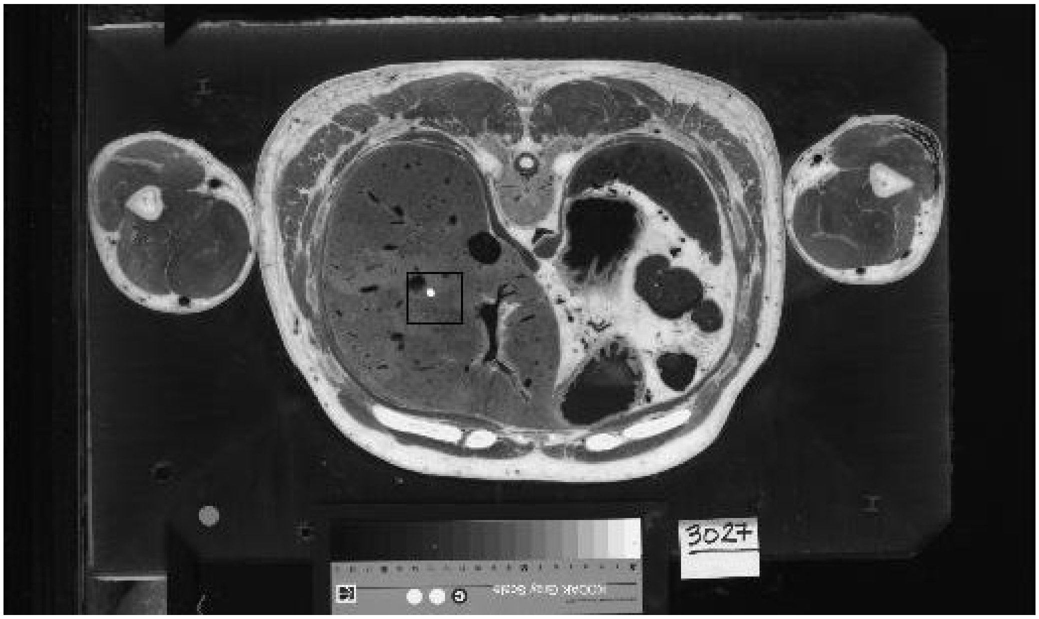

Figure 4.8: Cross section showing false segmentation enhanced in black box in the liver region.

segmented, the geometric area, A_{S_i}, of the segmented region from cross section I_i is calculated and compared to the area, $A_{S_{i+1}}$, of the next cross-section image's segmentation result. A *significant distinction* between the parameters A_{S_i} and $A_{S_{i+1}}$ indicate that an erroneous segmentation has occurred on the slice corresponding to cross section I_{i+1}. More precisely, a *significant distinction* is defined as at least a 16 percent decrease from A_{S_i} to $A_{S_{i+1}}$. Empirical testing has shown that a 16 percent difference produced acceptable re-segmentations, considering the male dataset cross sections were taken in an interval of 1mm.

4.3.4 Re-segmenting the cross section with new seed point

To correct this false segmentation, the cross section is segmented again with a different seed point resulting in the correct segmentation of the entire liver shown in Figure 4.9. In this section, we describe the process by which the new seed point is chosen.

Our algorithm automatically chooses another seed point in the neighborhood of the centroid. We first try to find a suitable seed within an $m \times m$ neighborhood of the centroid. If segmentation from any of these points does not result in a segmented region with an area close to the area of the segmented region that was extracted from the previous cross section, then another seed point is chosen from a larger neighborhood of the centroid. In our implementation, $m=3$ initially, and we expand the neighborhood window in one pixel increments (3x3, 4x4, 5x5, etc) until we locate a suitable seed point. This new seed is used for future segmentations of the remainder of the cross sections in

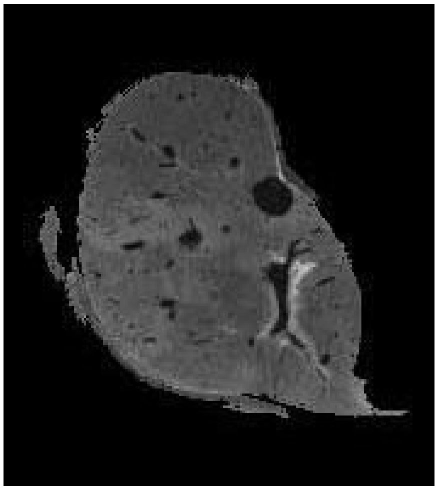

Figure 4.9: Liver region extracted from the re-segmentation from the cross section in Figure 4.8.

the sequence. If another problematic segmentation occurs, the same algorithm just described is used to select a new seed pixel.

4.3.5: Problem Two: The Adjacency Problem

Another major concern in region is the selection of the homogeneity criterion. Too small of a threshold value can lead to the region being under-segmented. Too big of a threshold value can lead to over-segmentation of the region of interest. The over segmentation of a region is referred to as the *adjacency problem* in this report. In medical images, over-segmentation results in one or more regions being segmented in addition to the region of interest.

4.3.6 Identifying the erroneous segmentation

The VHP data tells us that the slices were taken at a 1mm interval for the male dataset and a .33mm interval for the female dataset. Based on this fact, the algorithm assumes that the area of interest in slice i tends to be about the same size as the same area of interest in its adjacent slice $i+1$. If the area of a region of interest has grown to a size in pixels that is greater than 16% of the previous segmentation result, the slice is identified as resulting in an erroneous segmentation. Experimental results have proven that 16% is a reasonable limit. Figure 4.10a shows an image slice, i, from the male thorax dataset and the left lung region segmented from that slice in Figure 4.10b. The region in Figure 4.10b has an area of 6,346 pixels and was segmented with $\sigma=7$, the standard deviation of the intensity values in the image. Figure 4.11 shows the next image slice in the sequence, $i+1$, and the segmented lung region in Figure 4.12. This region has an area of 7,418 pixels and was segmented with $\sigma=7$. Figure 4.12 shows the tissue adjacent to the lung that was incorrectly identified as being part of the region.

Figure 4.10a: Original image from thorax region

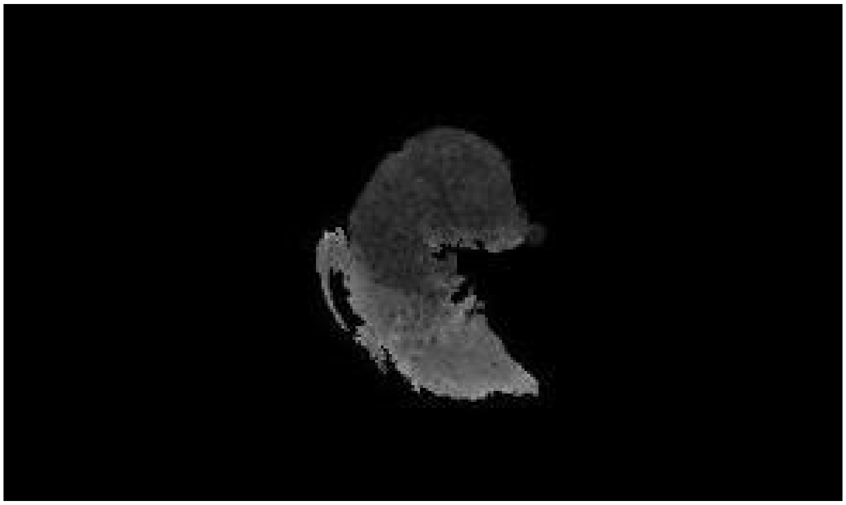

Figure 4.10b: Left lung segmented from Figure 4.8a

Figure 4.11: Next image in sequence following figure 4.10a

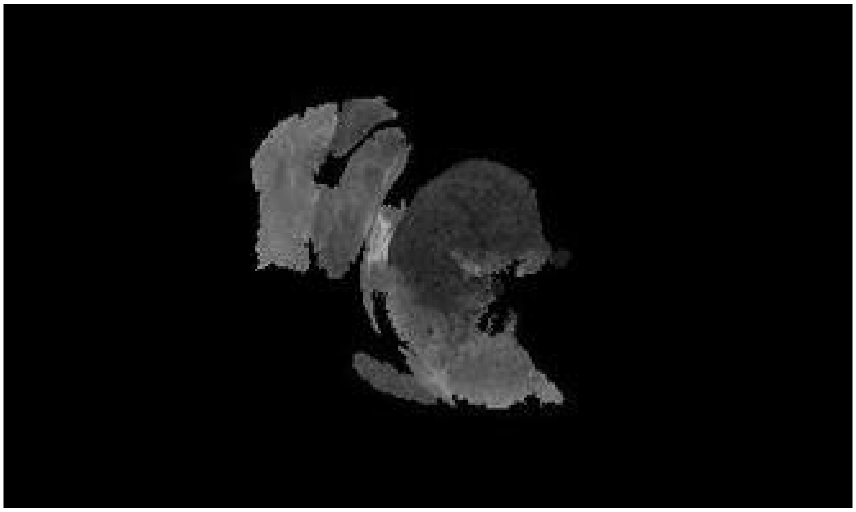

Figure 4.12: Incorrect segmentation of left lung

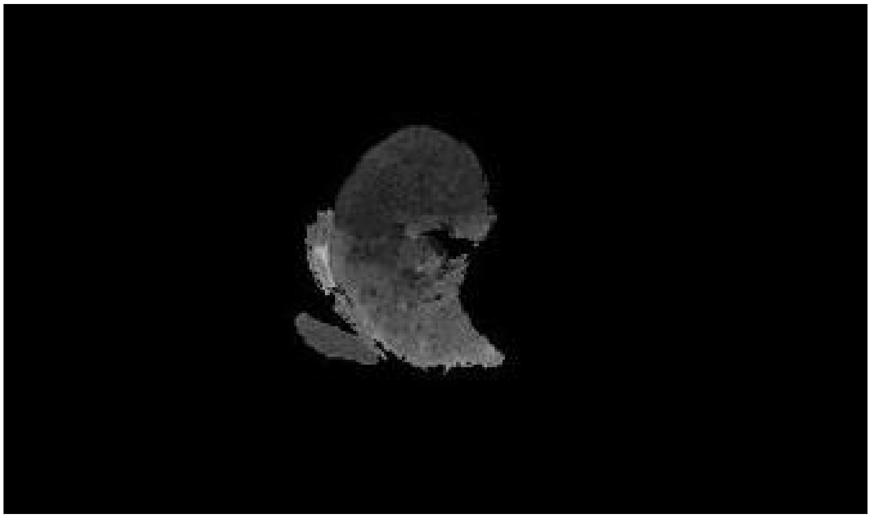

Figure 4.13: Segmented lung from Figure 4.12 after adjusting threshold value.

4.3.7 Re-segmentation With New Threshold Value

When over segmentation occurs, it is usually due to the threshold value of the homogeneity criterion. In this case when an erroneous segmentation occurs, the slice is segmented again using a stricter threshold value. The threshold value, σ**,** is decreased until the resulting segmentation has an area similar enough to the previous slice's segmentation. Similar enough is defined as less than a 16% area larger than the previous segmentation. Figure 4.13 shows the segmented lung after adjusting the threshold value. It has an area of 5,714 and was segmented with $\sigma = 5$. In Figure 4.13, the adjacent tissue was not segmented with the lung.

4.4. Image Post-processing

After the specified region is *grown*, a 2D image is created consisting of only the segmented region. The boundary-following operation in Figure 4.14 is then applied to this image to obtain an outline of the anatomical object of interest [5]. Generating outlines for segmented contours is a vital phase of image segmentation because the 3D visualization is highly dependent on the quality of the 2D extraction [6].

Next, a contour-filling algorithm is applied to the contour. Figure 4.15a is an image slice from the thorax region of the Visible Human dataset. Figure 4.15b represents the region of the right arm muscle tissue that was extracted using our technique. This result does not contain the white portion of the upper arm bone from the center of the muscle tissue because the bone's intensity values are not within the threshold used in the region growing algorithm. However, once the boundary-following and contour filling algorithms are applied to the initial segmented region, the pixels within the entire region of interest have the same intensities as the original cross section resulting in the image shown in Figure 4.15c.

The user initially chooses the seed for the first 2D cross section in the sequence. This is the only human interaction required for processing the cross sections. The centroid of the resulting segmented region is calculated and used as the seed point for the next cross section in the sequence. This process is repeated for successive cross sections in sequence. This seeded region growing procedure results in a collection of 2D images containing only the segmented region of interest in each image. This collection of images is joined together using the image processing program, ImageJ to form a 3D surface of the anatomical region of interest. Results from this method are presented in the next chapter and compared to other segmentation methods.

1. *Find the starting pixel* $s \in S$ *for the region using a systematic scan, say from left to right and from top to bottom of the image.*
2. *The current pixel in boundary following is denoted by* c *and the 4-neighbor to the west of* s *by* $b \in \bar{S}$. *Set* $c=s$.
3. *Let the eight 8-neighbors of* c *starting with* b *in clockwise order be* $n_1, n_2, \ldots, n_8$. *Find* n_i *for the first* i *that is in* S.
4. *Set* $c=n_i$ *and* $b = n_{i-1}$
5. *Repeat steps 3 and 4 until* $c=s$.

Figure 4.14: Boundary Following Algorithm

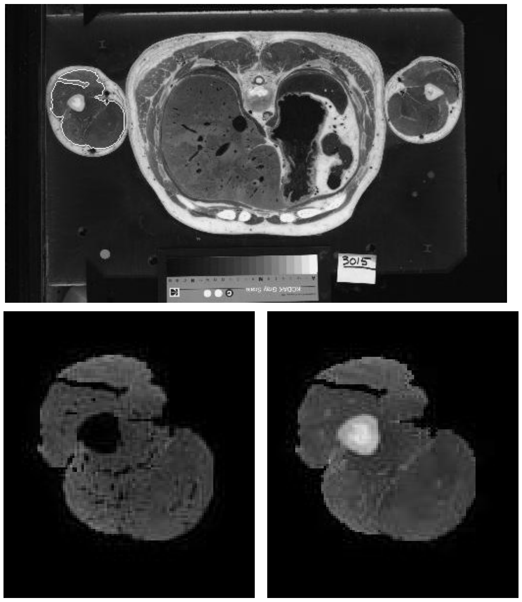

Figure 4.15. (a) Original cross section. (b) Segmented right arm muscle before contour filling. (c) Final result of segmented right arm muscle after applying the boundary-following and contour filling algorithms.

CHAPTER 5

THE EXPERIMENTS ON SEGMENTATION TECHNIQUES

5.1 Introduction

This chapter is dedicated to presenting the results of the segmentation technique discussed in chapter 3 as well as our technique used in MIST, presented in chapter 4.

5.2 Description of Test Images

The 110 test images used in the following experiments are taken from the Visible Human Project with permission under a license between Hamid Arabnia and The National Library of Medicine. Full color anatomical images are from the thorax and abdomen regions of the Male dataset. The images are stored as 24-bit 2046x1214 pixel RGB images in RAW format.

Color images can be separated into color components based on a specific model. Some of the common color models include red, green, blue (RGB), luminance, chrominance (YUV) and hue, saturation, intensity (HSI). In this study the images are decomposed into three parts representing each of the three components (i.e. red, green, blue for the RGB color model). Our application resizes the image proportionally to an 8-bit 512x302 pixel resolution image. The resolution is reduced so that more image slices can be kept in memory. The reduction from a 24-bit image to 8-bit image results in utilizing only the red component of the original RGB image to retain the color information, since information is lost when converting color images to grey-scale images. We expect to retrieve more detailed edge information than that retrieved from performing operations on grey-scale images. The original 10 test images are shown in Figure 5.1a-j. For each of the experiments in this section we attempt to segment the liver from the images. Figure 5.2 shows one test image outlining the ideal region to be segmented from all of the images.

5.3 Reconstruction Tool

The overall goal of this thesis is to use an appropriate segmentation technique to segment 2D regions to form one 3D object. The 3D objects are rendered using the free source toolkit, ImageJ, using the stack of 2D segmentations as input into the application. ImageJ was developed by Wayne Rasband at the Research Services Branch, National Institute of Mental Health in Bethesda, Maryland. In addition to 3D projections, ImageJ can display, edit, analyze, process, save and print 8-bit, 16-bit and 32-bit images. It can read many image formats including TIFF, GIF, JPEG, BMP, DICOM, FITS and "raw". It supports "stacks", a series of images that share a single window. ImageJ was designed with an open architecture that provides extensibility via Java plugins that can be written with its built in editor and Java compiler. User-written plugins make it possible to solve almost any image processing or analysis problem [4].

5.4 The Experiments using Newman, et. al. Technique

This section will provide experiments based on the segmentation algorithm proposed by Newman, et al., and described in Chapter 4.

5.4.1 Implementation Details

Several adjustments were made in our implementation of Newman's algorithm. First, the median is computed on a two-dimensional 3x3 window instead of a three-dimensional 3x3x3 window as described in their implementation. Also, where they used

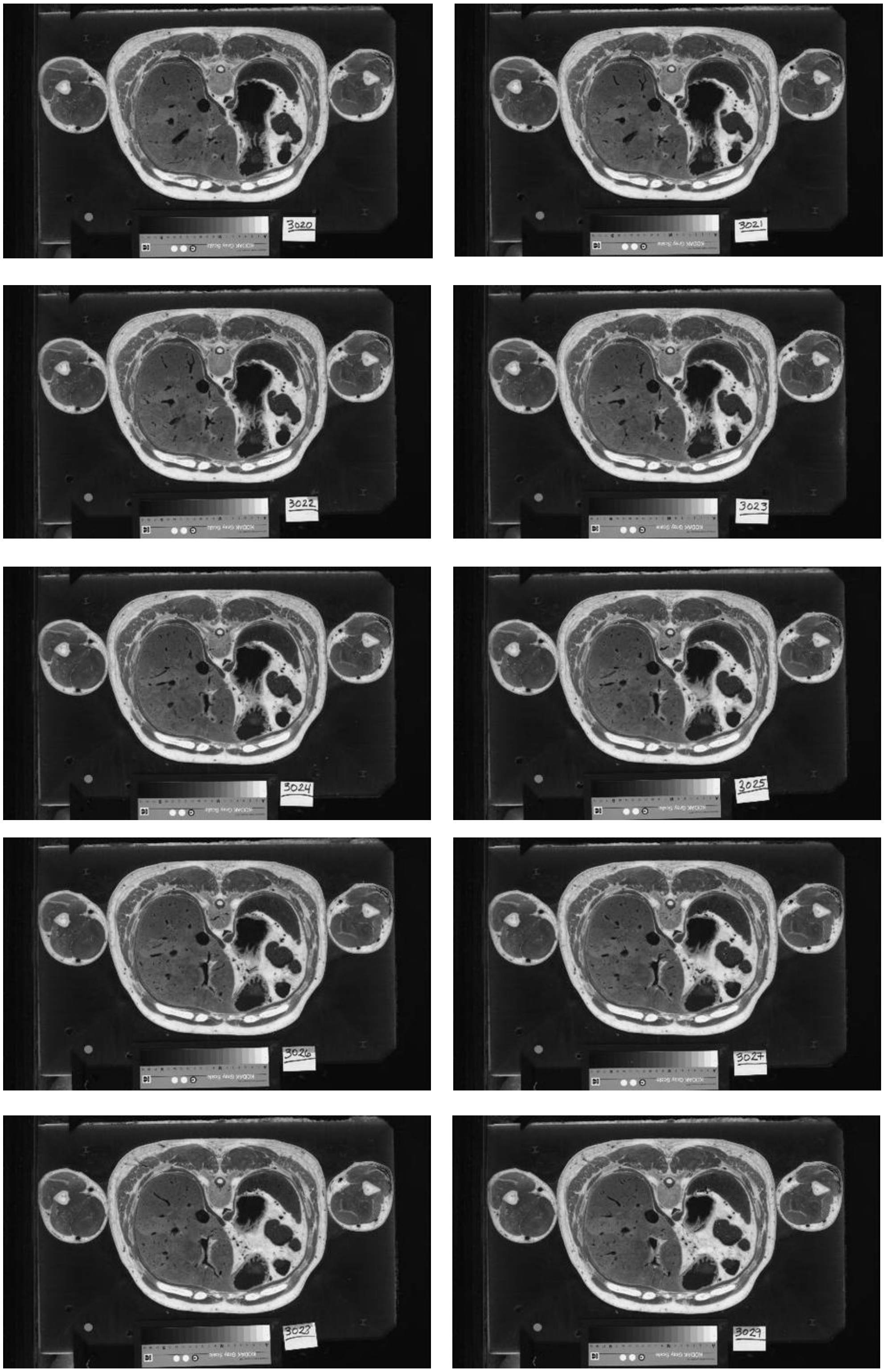

Figure 5.1a-j: The set of 10 sequential 2D test images used for experiments.

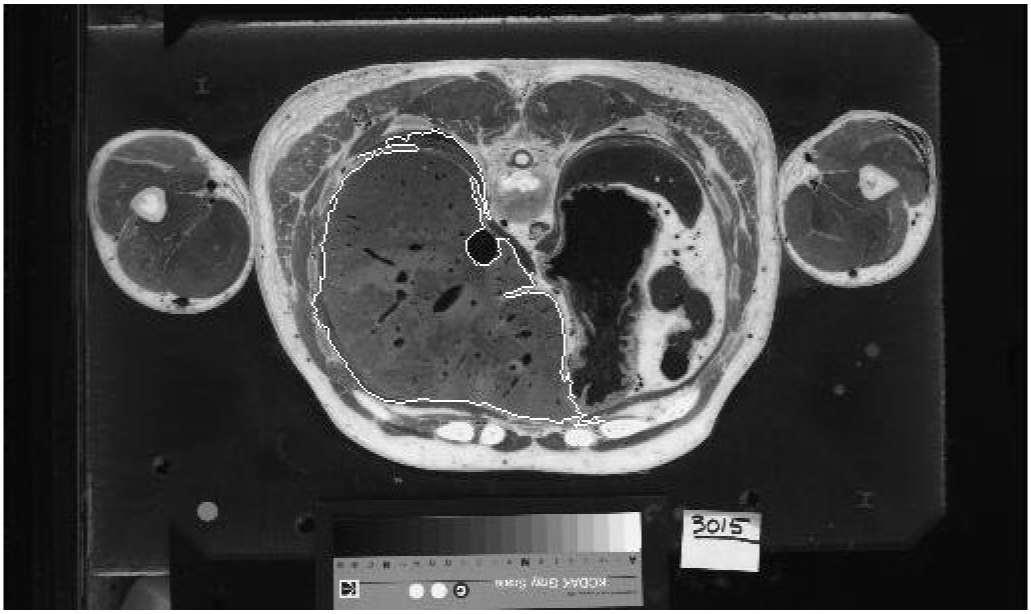

Figure 5.2: Test image with ideal segmentation outlined

specific static values for thresholds in the region growing process, depending on the type of tissue to be segmented, in our implementation we used a threshold equal to the standard deviation for each image in the sequence. Lastly, Newman describes a 3D close morphological operation used in the post processing of the initial segmentations. We use 2D close operation on the segmentations.

5.4.2 Results

Figures 5.3 and 5.4 show the results of this technique as described above. Each image is shown in binary and grayscale. The region that is segmented is significantly smaller than the correct segmentation. Due to these results, we decided to increase the threshold value used in the region growing algorithm to twice the standard deviation. This subtle change makes a significant difference in the segmentations, shown in the results in Figures 5.5 and 5.6. The regions segmented are closer in size to the correct segmentation.

5.4.3 Problems

There are several disadvantages of the Newman algorithm. First, there is an issue with discontinuity. The post processing techniques could result in a separation of the region of interest as shown in [9]. For our application of the segmentations, we only want to segment one region of interest from each image to produce the 3D visualization. If the segmentation results in more than one region segmented from the image, it would create problems in our final reconstruction. The next problem associated with this technique is the amount of gaps and hole artifacts present in the segmentations. These issues do not lead to a realistic 3D visualization of the organ or tissue, as shown in

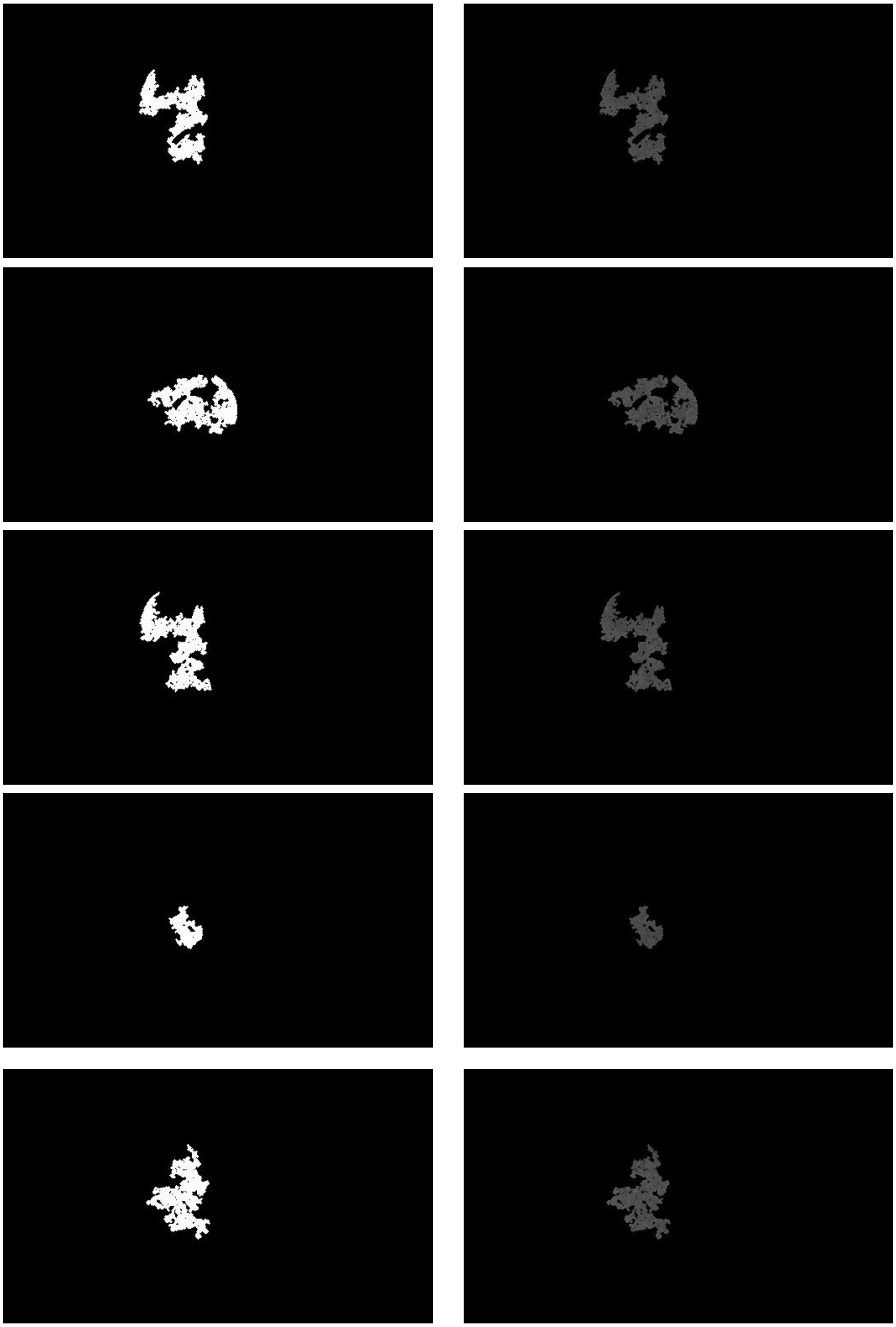

Figure 5.3a-j: The results from running Newman Segmentation algorithm on the first 5 test images. Each set of images represents the binary and grayscale results.

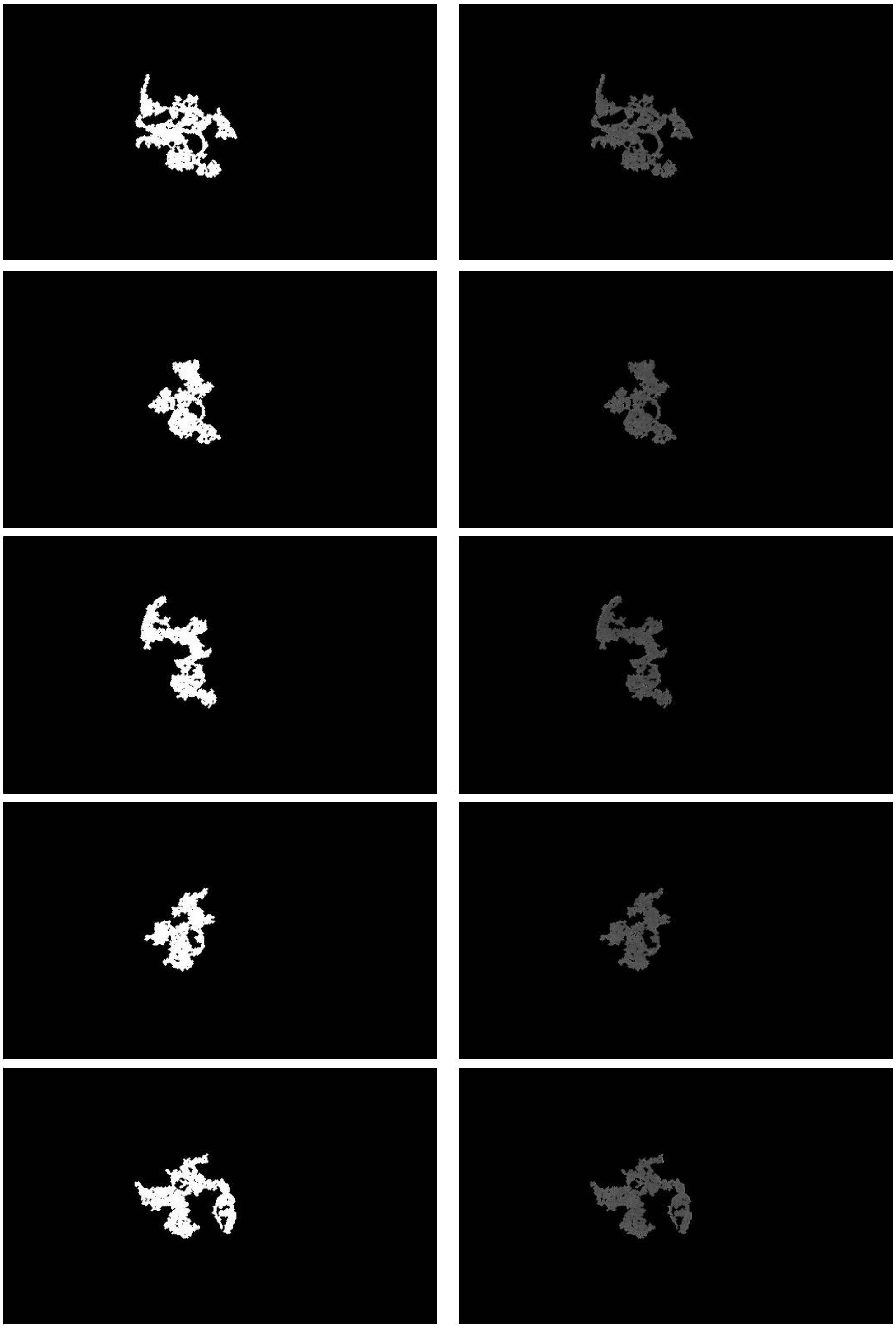

Figure 5.4a-j: The results from running Newman Segmentation algorithm on the remaining 5 test images. Each set of images representsthe binary and grayscale results.

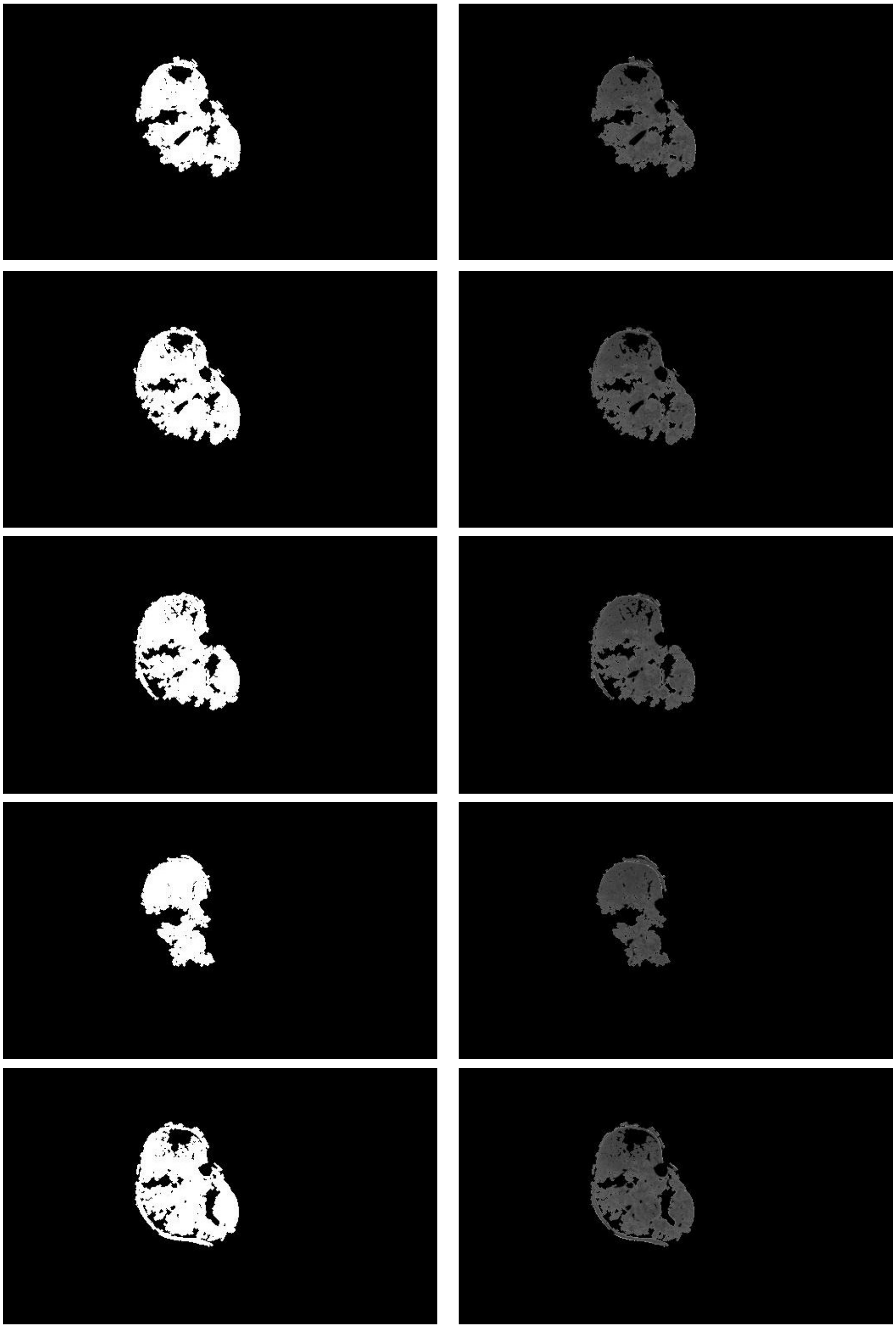

Figure 5.5a-j: The results from running the modified Newman segmentation algorithm on the first 5 test images. Each set of images represents the binary and grayscale results.

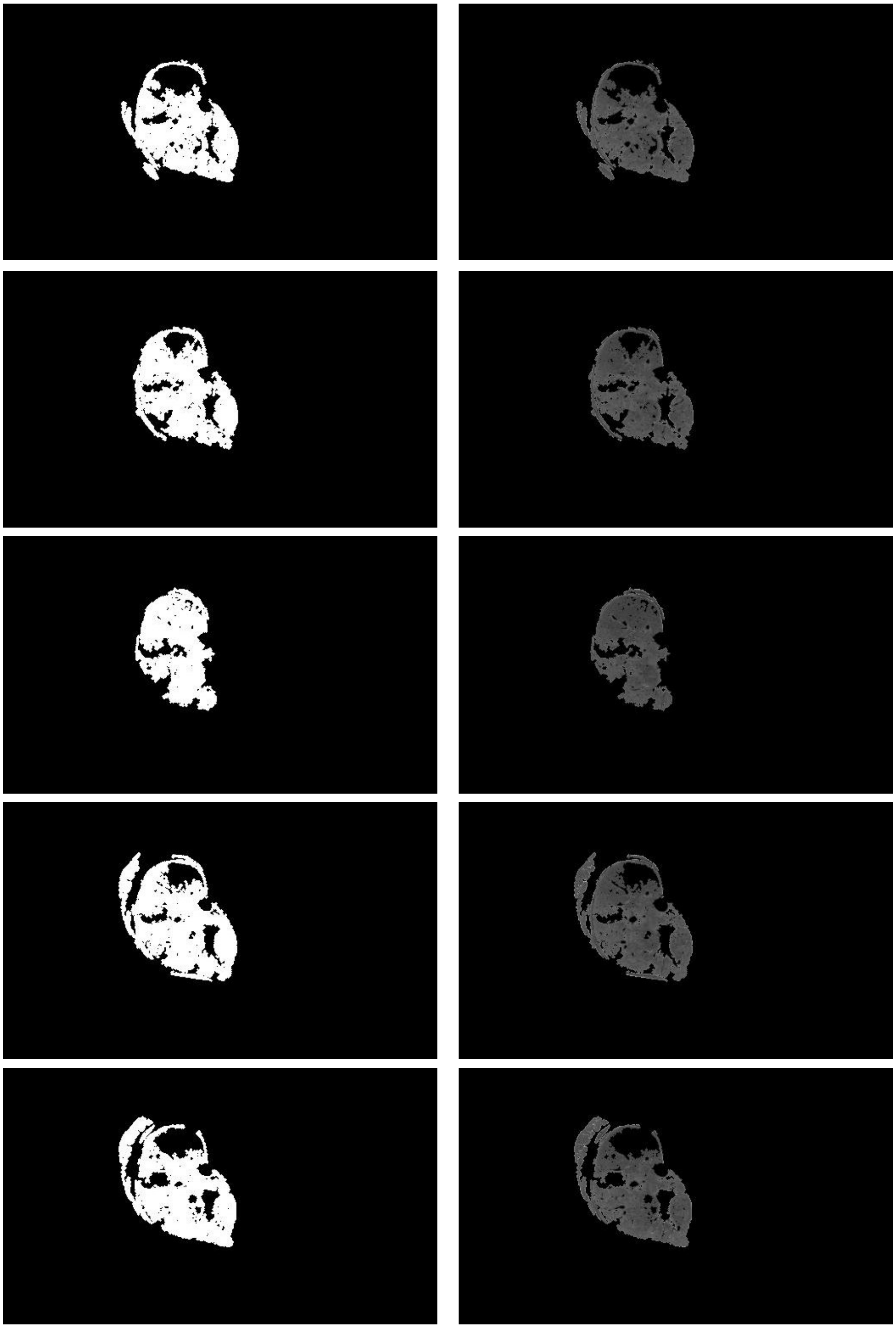

Figure 5.6a-j: The results from running the modified Newman segmentation algorithm on the remaining 5 test images. Each set of images represents the binary and grayscale results.

Figure 5.7. The next section shows how our MIST technique addresses the problems of the Newman technique.

5.5 The Experiments using MIST

This section is dedicated to showing how the MIST algorithm evolved into its final state. The experiments conducted in this section use a seeded region growing algorithm. The region is grown using the threshold, σ , equal to the standard deviation of each input image in the sequence. The idea is to segment the same anatomical feature from each of the sequential 2D images. To accomplish this task, the center of mass of a segmented region is used as the seed point for the next image in the sequence. These 2D segmentations are joined together using ImageJ, to create a 3D visualization of the object of interest.

5.5.1 Experiment One: Basic Region Growing Algorithm

A basic region growing algorithm is used for the experiments in this section. No additional processing is performed on the input images. Ten sequential test images and their respective binary two-dimensional segmentations are shown in Figure 5.8a-j.

The coarse segmentation results presented do not prove sufficient for adequately visualizing the region of interest. There are gaps and holes in the segmentations. This leads to some of the very small sub regions being segmented as the region of interest, identified as the *centroid problem* in Chapter 4. Figure 5.8d, 5.8h, and 5.8i resulted in a small sub-region being segmented. Also, adjacent tissues are segmented as part of the object of interest. We refer to this problem as the *adjacency problem.* This is evident in Figure 5.8c. These inconsistencies that are present in the 2D segmentations do not give the user a realistic model of the object of interest.

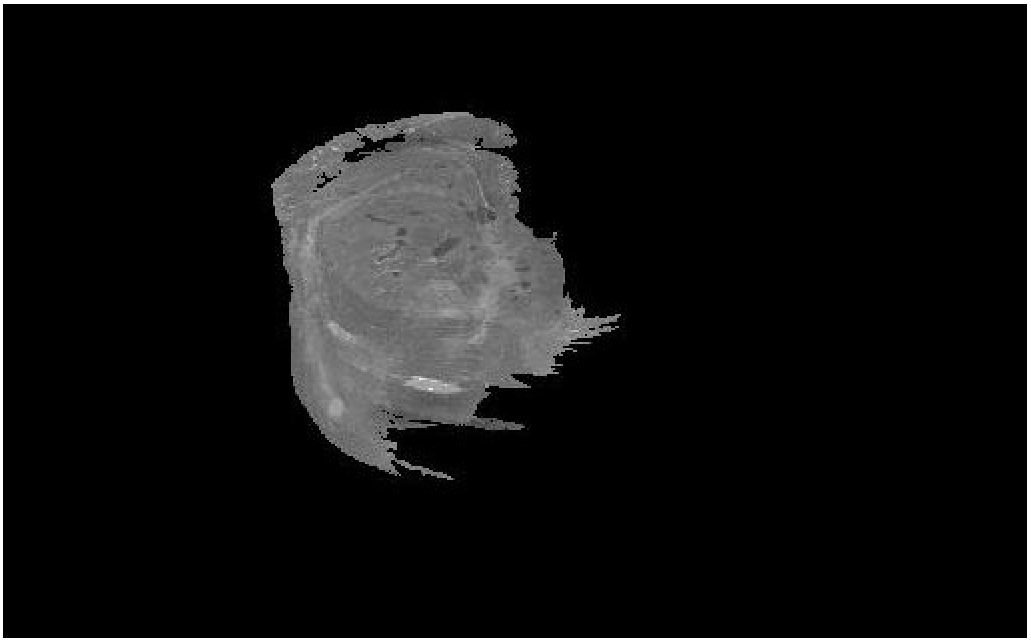

Figure 5.7: 3D projection of all 110 test image segmentations using the Newman algorithm.

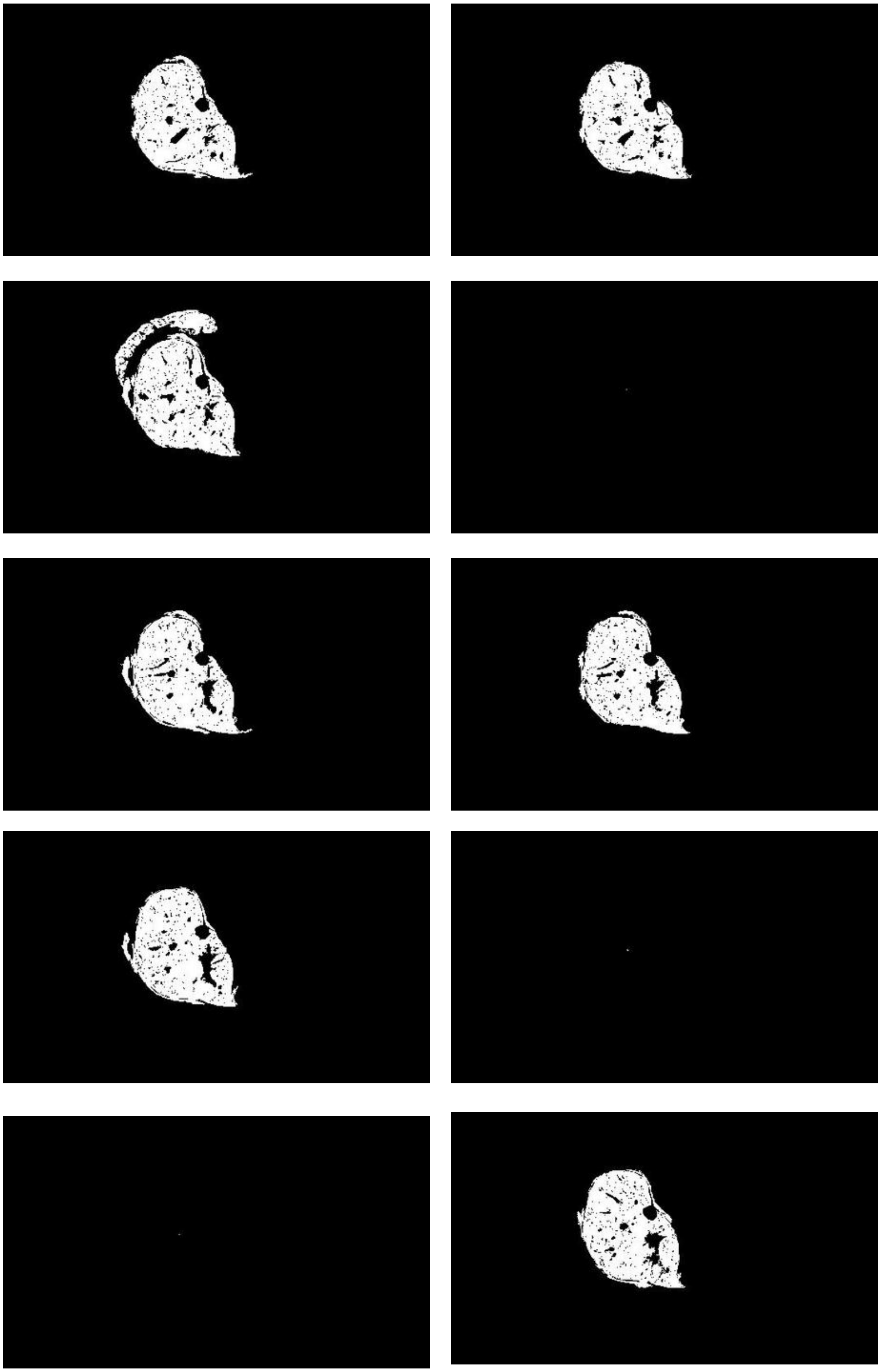

Figure 5.8: Results from running basic region growing algorithm on ten test images.

5.5.2 Experiment Two: Region Growing with Contour Filling

For this set of experimental results, a basic region growing algorithm is used with the additions of the boundary following and contour filling algorithms described in Chapter 4. The contour filling function is performed on resulting segmentations after the region growing step. The entire region enclosed by the region boundary is considered part of the segmented region. The code that addresses the *centroid problem* was also added for the experiments in this section. The 2D segmentations are show in Figures 5.9 and 5.10. Each of the ten test images are shown in binary and grayscale.

This algorithm is proven effective to significantly reduce the amount of gaps and holes that were present in the previous section's segmentations. These inconsistencies are no longer present in the 2D segmentations in Figures 5.9 and 5.10. The segmentations produced from this method are more realistic than the segmentations from the previous section. However, the *adjacency problem* still exists.

Table 5.1 shows the statistics for the area of the segmented regions in Experiments One and Two. The user supplies the seed point for test image 1 and successive seed points are at the location of center of mass in the previous segmented region. We are able to see how the addition of the contour filling process, along with the code that solves the *centroid problem* in Experiment Two corrects the incorrect segmentations for images 4, 8, and 9. The sizes of the segmentations in Experiment Two are more consistent than those in Experiment One, as denoted by the area columns in Table 5.1.

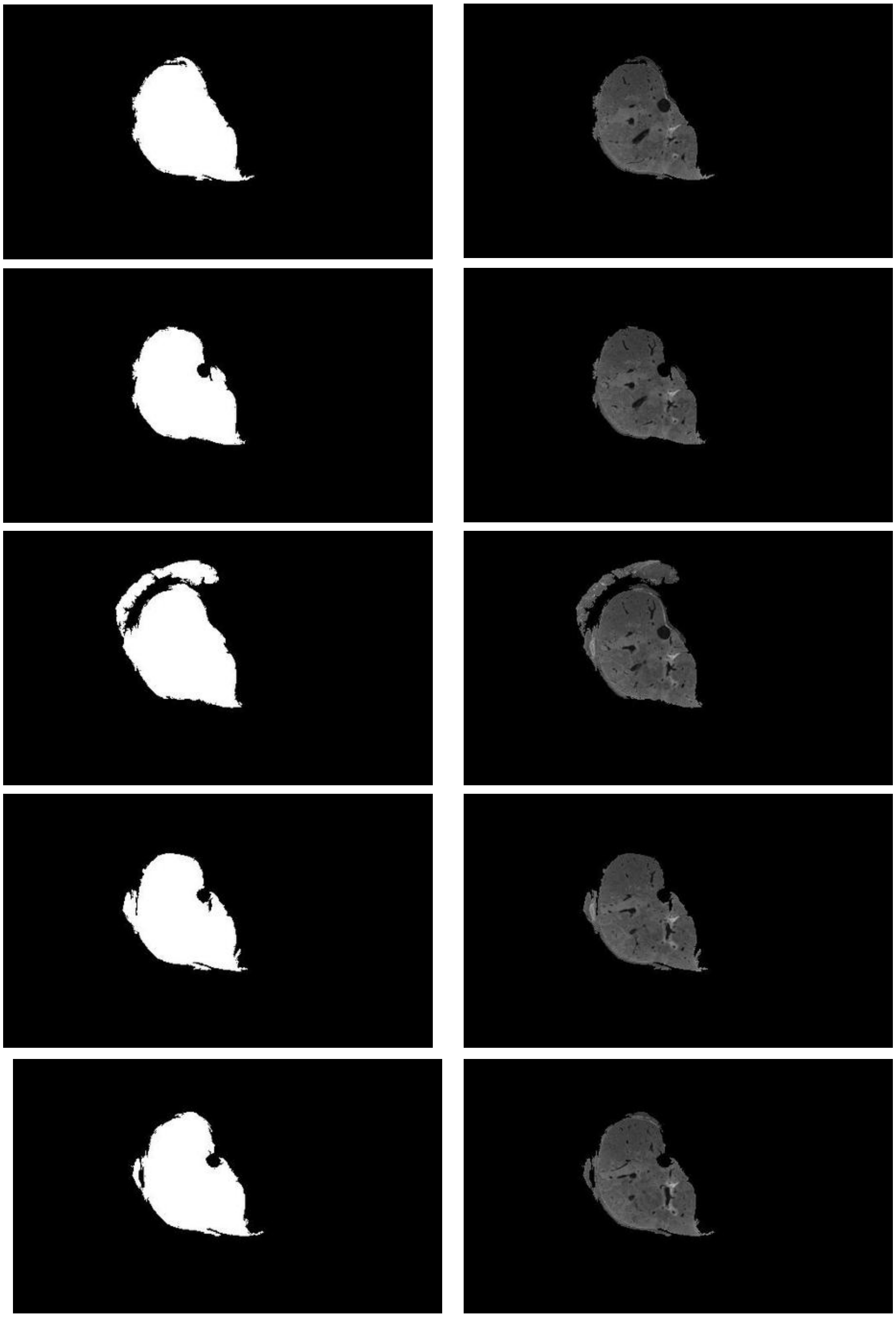

Figure 5.9: Results of the region growing and contour filling operations applied to the first 5 test images. Images are the binary and corresponding grey scale image

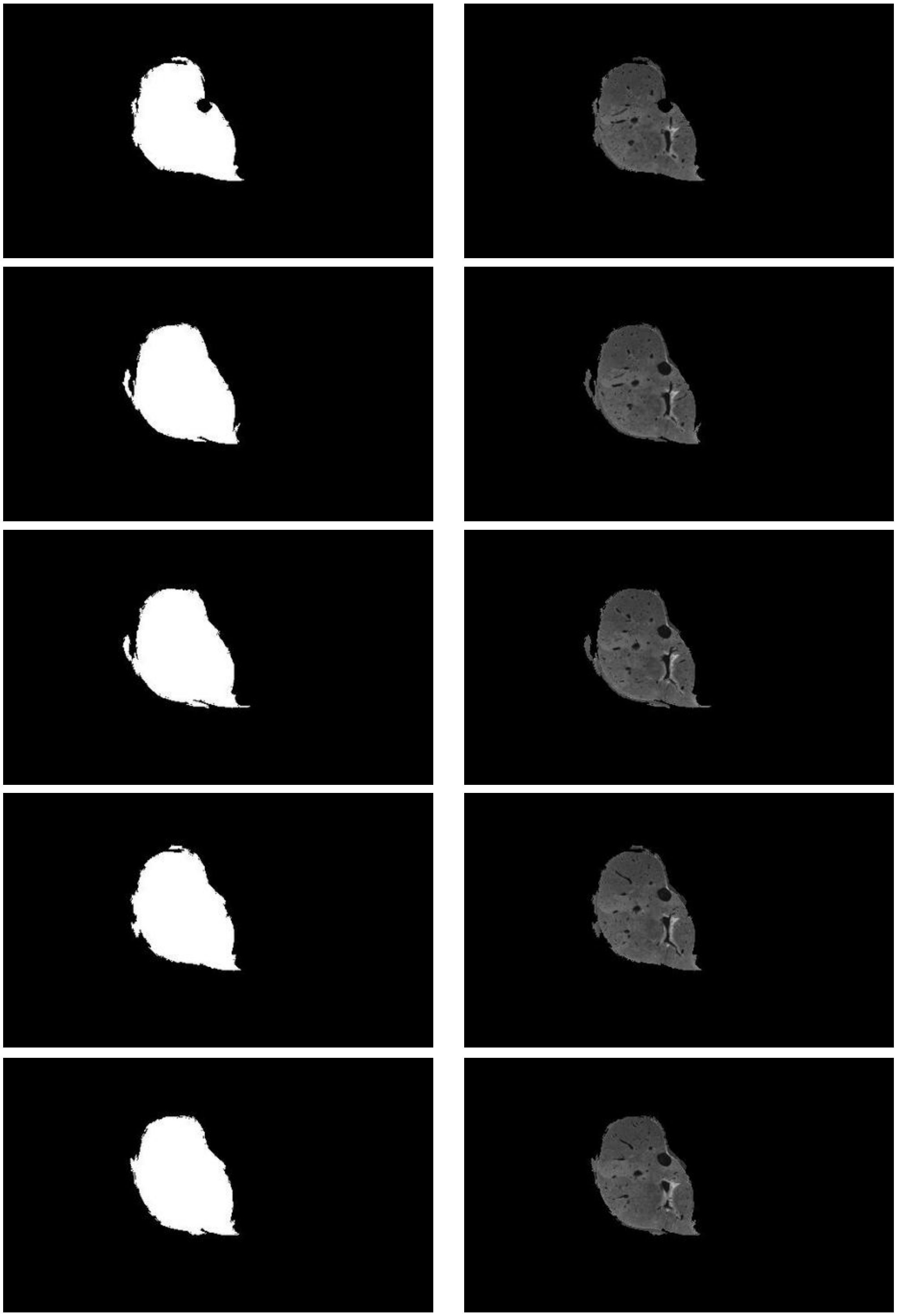

Figure 5.10: Results of the region growing and contour filling operations applied to the remaining 5 test images.

TABLE 5.1: Comparing Area of segmented regions from Experiments One and Two

Image Number	**Seed Point for Experiment One**	**Area of Region after Experiment One, in pixels**	**Seed Point for Experiment Two**	**Area of Region after Experiment Two, in pixels**
1	(198, 160)	11,647	(198, 160)	12,984
2	(214, 143)	11,176	(215, 143)	12,315
3	(213,144)	11,381	(213, 145)	15,675
4	(210, 130)	1	(209, 129)	12,597
5	(212,145)	11,623	(212, 145)	12,961
6	(212, 145)	11,098	(212, 143)	12,383
7	(211, 143)	11,415	(213, 143)	13,038
8	(211, 143)	3	(213, 143)	12,966
9	(211, 142)	1	(213, 144)	12,733
10	(211, 142)	10,942	(213, 141)	12,623

5.5.3 Experiment Three: MIST Algorithm

This set of experimental results are produced by the final MIST algorithm which tackles the *adjacency problem*, not addressed by the algorithms in the previous sections. The method used to correct the segmentations that identified adjacent tissues as part of the object of interest is described in detail in Chapter 4. Figures 5.11 and 5.12 show the 2D segmentations that result from using the MIST algorithm

The resulting 3D reconstruction, shown in Figure 5.13 is the most realistic as compared to the results from the previous sections. There are no gaps and holes in the 2D segmentations and no adjacent regions are identified as part of the region of interest.

5.5.4 Experiment Four: Modified MIST Algorithm

Though the segmentations in Figures 5.11 and 5.12 are the most realistic so far in our experiments, we recognized that the boundary could be visually improved by applying the same morphological operators as the researchers in [7,9]. While Newman used a close operation followed by dilation, we use only a dilation operation. This is because the close operation was used in Newman's algorithm to remove isolated interior pixels, which correspond to the gaps and holes in the segmentations. Using the boundary following algorithm and enclosing the contour solves this problem in our algorithm, so there is no need to use the close operation in our implementation. The resulting segmentations are shown in Figures 5.14 and 5.15. The enhancements are not as noticeable in the 2D segmentations, but they are clearly visible in the 3D reconstruction in Figure 5.16.

The modifications made to the MIST algorithm were needed in order for the 3D reconstruction, to be as realistic as possible. In Table 5.2, we see that these modifications

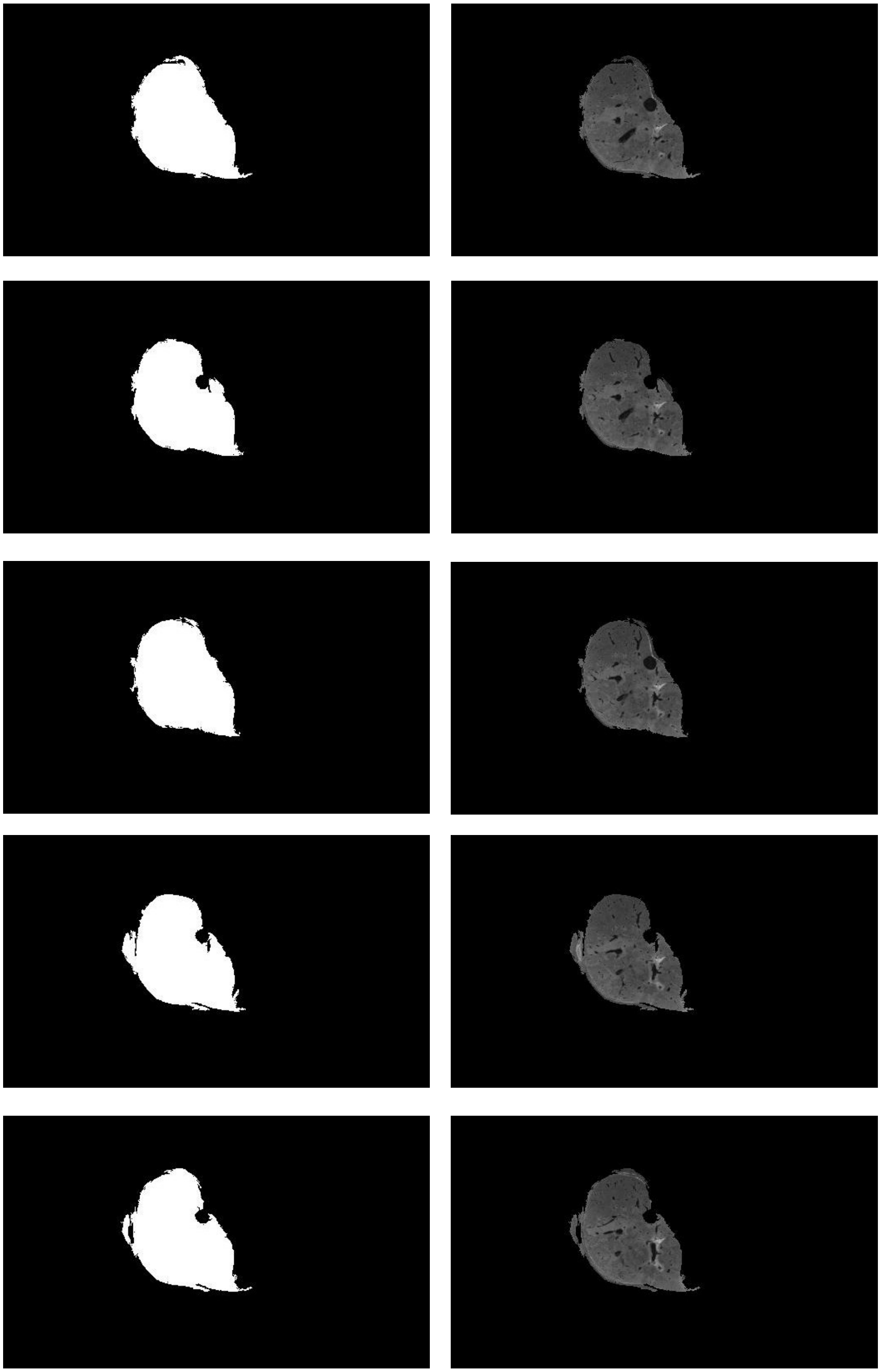

Figure 5.11: Results of the MIST algorithm applied to the first 5 test images.

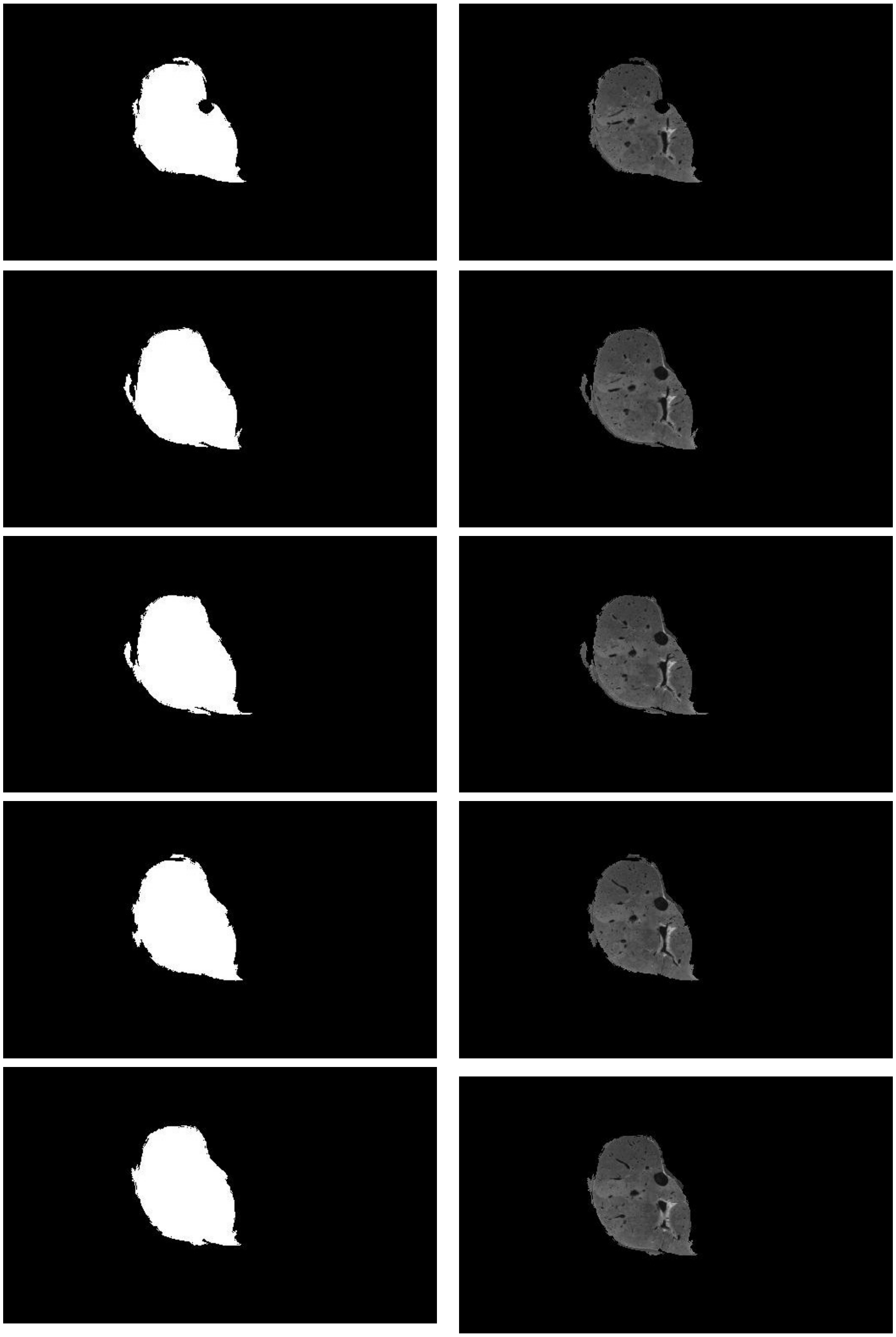

Figure 5.12**:** Results of the MIST algorithm on the remaining 5 test images.

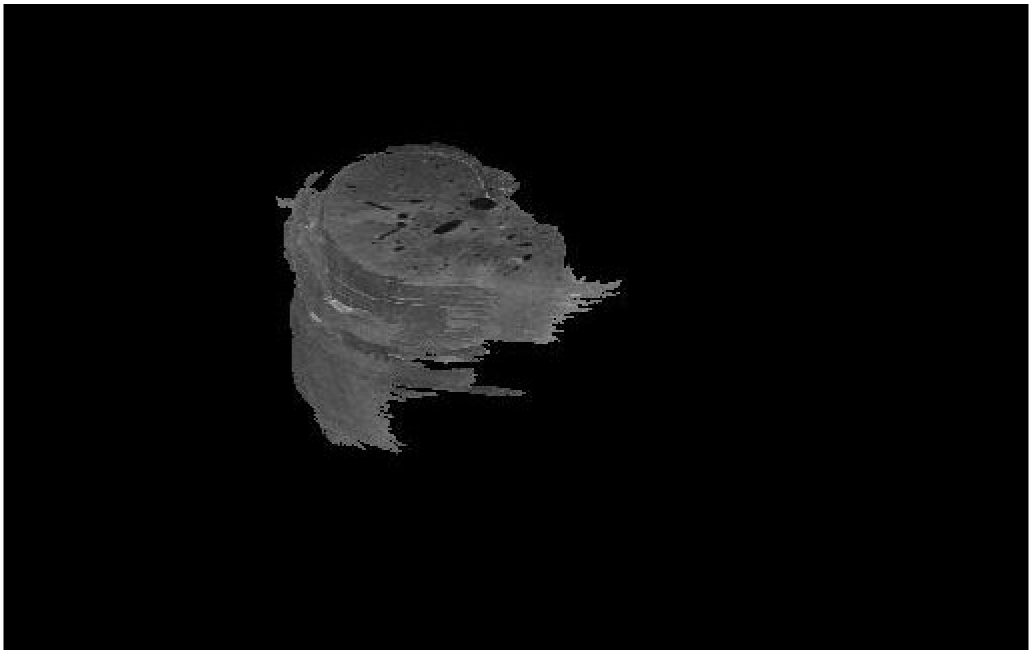

Figure 5.13: 3D projection of all 110 test image segmentations using MIST algorithm.

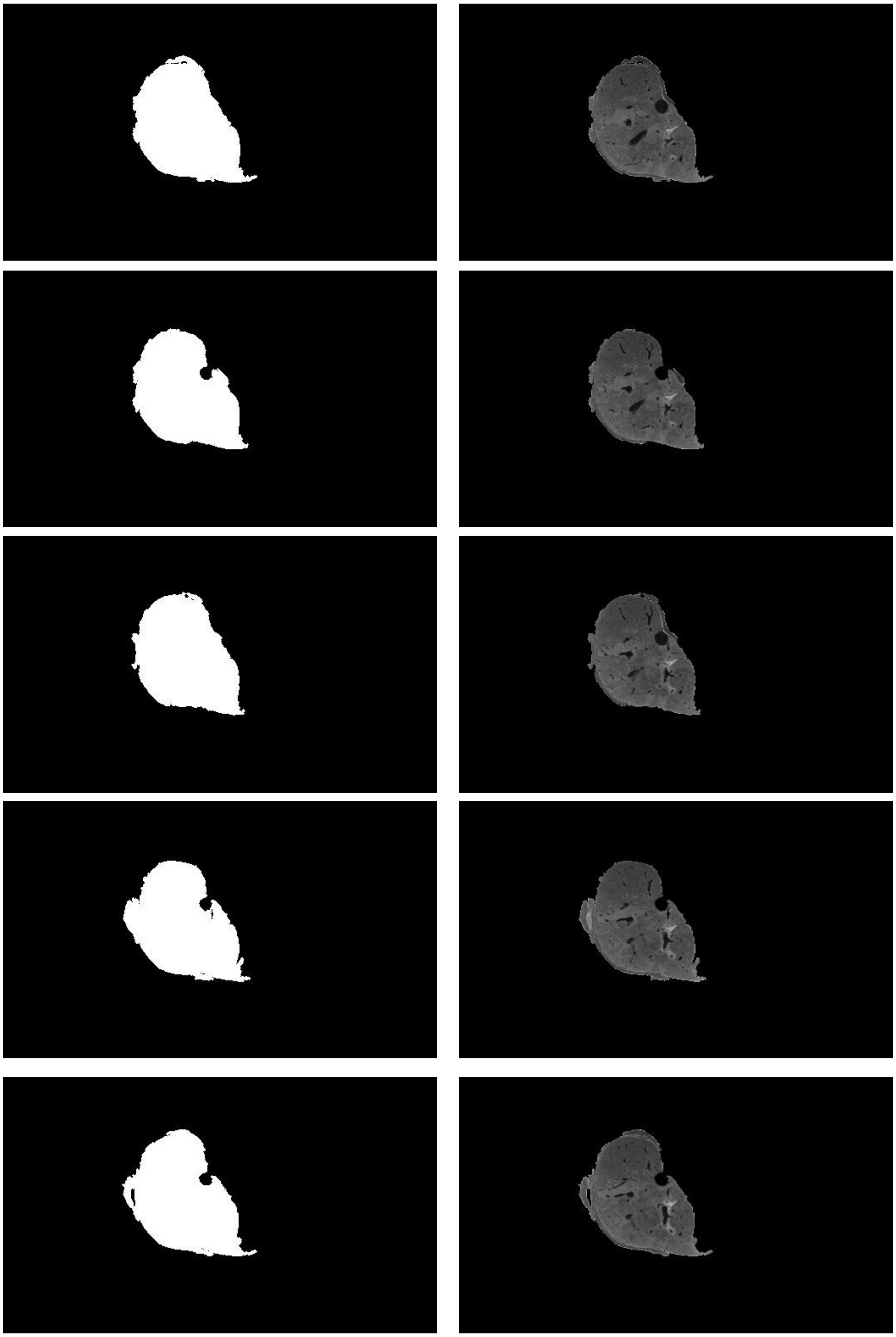

Figure 5.14: Results of the modified MIST algorithm on 5 test images.

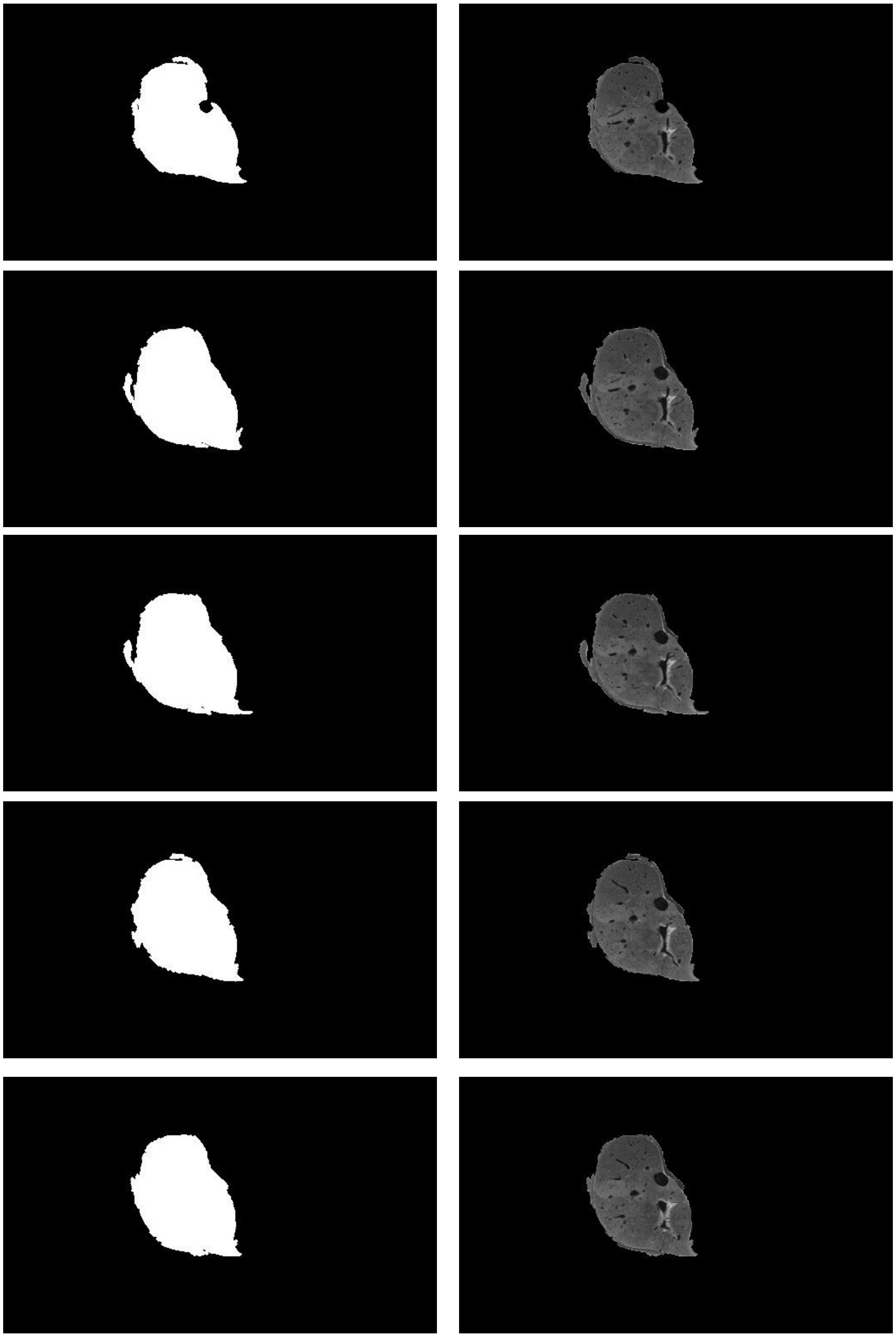

Figure 5.15: Results of modified MIST algorithm on remaining test images

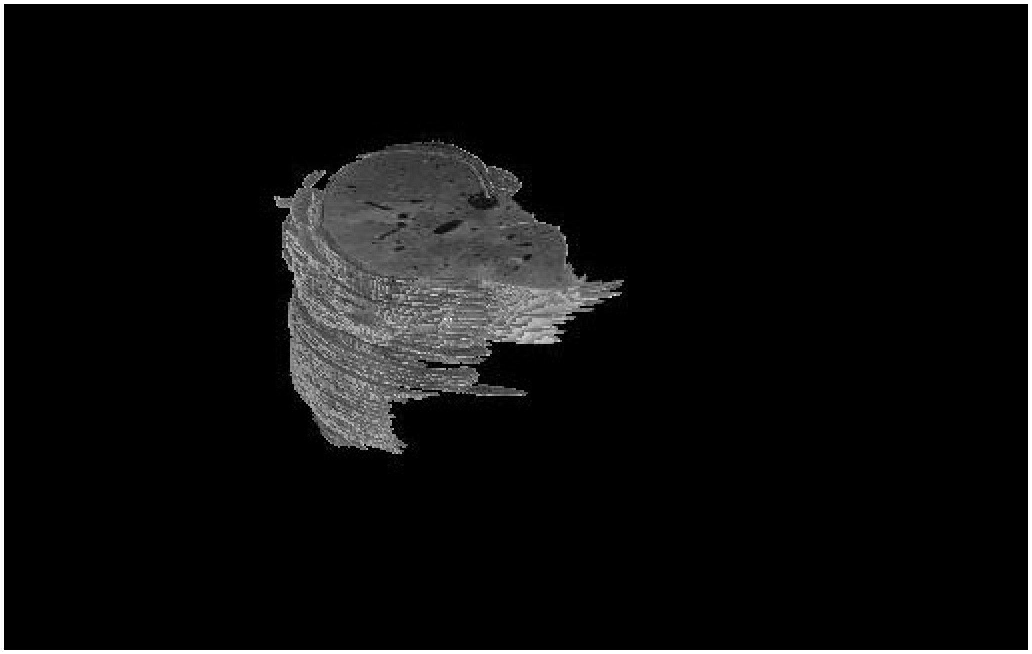

Figure 5.16: 3D projection of segmentations of 110 test images using modified MIST algorithm.

Table 5.2 Area of segmented regions in Experiments Three and Four

Image Number	**Area of Region after Experiment Three, in pixels**	**Area of Region after Experiment Four, in pixels**
1	12,984	13,603
2	12,315	12,866
3	12,466	13,033
4	12,597	13,269
5	12,961	13,662
6	12,383	13,001
7	13,038	13,631
8	12,966	13,589
9	12,733	13,287
10	12,623	13,153

do not alter the size of our segmentations by a significant amount. This ensures us that the segmentations from the modified MIST algorithm produced segmentations with consistent sizes as the segmentations resulting from the MIST algorithm in Experiment Three.

5.6 Conclusion

The MIST algorithm corrects the issues faced with Newman's algorithm. Region growing guarantees the segmentation of a connected closed contour, while the use of the contour filling operation ensures that the segmented region of interest is free of gaps and hole artifacts unlike the segmentations produced by Newman et al. In this chapter we have presented results from the segmentation results produced by Newman's algorithm as well as in each step of our proposed MIST algorithm. Experimental results show that our MIST method performs better for whole organ and tissue segmentations.

CHAPTER 6

CONCLUSIONS AND FUTURE WORK

Segmentation of the Visible Human Dataset offers many additions to the original goal of a three-dimensional representation of a computer generated anatomical model of the human body and to the general study of human anatomy. In this paper, we have presented a new automatic region growing algorithm called the Medical Image Segmentation Technique (MIST) that improves image segmentation of 2D contours for the purpose of reconstructing 3D anatomical structures. It is our first attempt to address the issue of segmenting organs, tissue and other structures from color anatomical images.

Seeded region growing offers several advantages over conventional segmentation techniques. Unlike gradient and Laplacian based edge detection methods, a region found by region growing is guaranteed to be connected and consist of a one pixel thick boundary, since we only add pixels to the exterior of our region. MIST addresses the *adjacency problem*, therefore the segmented region will never contain too much of adjacent tissues, as long as the parameters are defined correctly. In addition, our technique guarantees that he seed is contained in the region by addressing what we call the *centroid problem*, unlike the method presented in [10]. We have compared the results from MIST with papers attempting to achieve the same goals. In our experiments, our method proved to perform better and produce better 3D visualizations.

Several enhancements need to be investigated. Improved 3D visualization from the segmented regions can be achieved by combining the full color anatomical images with the corresponding CT images in the dataset to get a more realistic 3D model of organs and tissues in the human body. Another area of future work is to combine data with knowledge and provide semantic meaning to the images, as the National Library of Medicine is striving to accomplish.

REFERENCES

[1] Ackerman M.J., “Fact sheet: The Visible Human Project”, National Library of Medicine, 1995.

[2] Revol-Muller C., et al. “Automated 3D region growing algorithm based on an assessment function”, *Pattern Recognition Letters*, 2002, 23, pp. 137-150.

[3] Haralick, R.M., and Shapiro, L.G. “SURVEY: image segmentation techniques”, *Computer Vision Graphics Image Processing*, 1985, 29, pp. 100-132.

[4] http://rsb.info.nih.gov/ij/

[5] Jain R. et al, *Machine Vision*, McGraw-Hill, Inc. 1995.

[6] Imelinksa C., Downes, M.S., and Yuan, W, “Semi-Automated color segmentation of anatomical tissue”, *Computerized Medical Imaging and Graphics*, 2000, 24, pp. 173-180.

[7] Newman, T., Tang, N., Bacharach, S., and Choyke, P., “A volumetric segmentation technique for diagnosis and surgical planning in lower torso CT images”. In: *Proc. 13th International Conference on Pattern Recognition*, Vienna, 1996, pp. C-553 – C-557.

[8] Ruzon and Tomasi. “Color Edge Detection with the Compass Operator”. *Pattern Recognition*, 1999, 2, pg 160-166.

[9] Newman, T., Tang, N., Dong, C., and Choyke, P., “Slice-adaptive histogram for improvement of anatomical structure extracting in volume data”, *Pattern Recognition Letters*, 2002, 23, pp. 25-38.

[10] Revol, C., and Jourlin, M., "A new minimum variance region growing algorithm for image segmentation", *Pattern Recognition Letters*, 1997, 18, pp. 249-258.

[11] Myler, H., and Weeks, A., *The Pocket Handbook of Image Processing Algorithms in C*, PTR Prentice Hall, Inc. 1993.

[12] Vliet, L., Young, I., and Beckers, G., "An edge detection model based on non-linear laplace filtering", *Pattern Recognition and Artifical Intelligence*, 1988, pp. 63-73.

[13] Vliet, L., and Young, I., "A nonlinear Laplace operator as Edge Detector in Noisy Images", *Computer Vision, Graphics, and Image Processing*, 1989, 45, pp. 167-195.

[14] Lee, J.S.L., Haralick, R., and Shapiro, L., 'Morphologic Edge Detection", *Proc. 8th International Conference Pattern Recognition*, Paris (France), 1986, pp. 369-373.

[15] Sonka, M., Hlavac, V., and Boyle, R., 'Image Processing, Analysis, and Machine Vision", Brooks/Cole Publishing Company, 1998.

[16] Zucker, S. W., 'Region growing: Childhood and adolescence", *Computer Graphics and Image Processing*, 1976, 5, 382-399

[17] Asano, T., and Yokoya, N., 'Image segmentation schema for low-level computer vision", *Pattern Recognition*, 1981, 14, pp. 267-273.

[18] Pal, N., and Pal, S., "A Review on Image Segmentation Techniques", *Pattern Recognition*, 1993, 26, pp. 1277-1294.

[19] C.Johnson, R.MacLeod, & J.Schmidt, "Software Tools for Modeling, Computation, and Visualization in Medicine", *CompMed 94 Proceedings*, World Scientific, 1995.

[20] Bessaud, Jean-Christophe et. al, 'The Visible Human Slice Sequence Animation Web Server", *Proc. The 3rd Visible Human Project Conference*, Bethesda, Maryland, USA 2000.

[21] Gerlach, Sebastian. et al., 'The Real-Time Interactive Visible Human Navigator", *Proc. The 3rd Visible Human Project Conference*, Bethesda, Maryland, USA, 2000.

[22] Yuh-Jye Chang, Paul Coddington and Karlie Hutchens, "Viewing the Visible Human using Java and the Web", *Proc. of Asia Pacific Web (APWeb) '98*, Beijing, Sept 1998, eds. Y. Yang et al., (International Academic Publishers, 1998).

[23] http://anatquest.nlm.nih.gov/Anatline/GenInfo/index.html

[24] P.Gingins, P.Kalra, P. Beylot, N.Magnenat-Thalmann, J. Fasel, "Using VHD to build a comprehensive human model"**,** *Proc. The Visible Human Project Conference,* Bethesda, Maryland,USA, 1996.

[25] http://www.visembryo.com/

[26] Bottcher P, Maierl J, Schiemann T, Glaser C, Weller R, Hoehne KH, Reiser M, Liebich H., 'The Visible Animal Project: a three-dimensional, digital database for high quality three-dimensional reconstructions", *Veterinary Radiology and Ultrasound*, 1999, 40, pp 611-616.

[27] Imielinska, C. et al., ‘Hybrid Segmentation of the Visible Human Data”, *Proc. The 3rd Visible Human Project Conference*, Bethesda, Maryland, USA, 2000.

APPENDIX

LIST OF PROGRAMS

The files related to the thesis are listed below:

README : Explains the usage of the program files.

commandLineIO.java : The class file containing methods for reading and writing to standard output.

edgedetect.java : The class file containing the edge detector operators.

edgeDetectDriver.java: The driver file for the standard edge detector operators

ImageIO.java : The class file containing methods for reading and writing images.

iterative.java : The class file containing the region growing algorithms.

MIST_driver.java : The driver file for the MIST technique.

NLL_driver.java : The driver file for the Non-linear lapace operator.

Point.java : The class file defining a pixel in a image.

TS_driver.java : The driver file for the Newman segmentation technique.